AD_____

Award Number:
W81XWH-09-1-0410

TITLE:
Harnessing the power of light to see and treat breast cancer

PRINCIPAL INVESTIGATOR:
Nirmala Ramanujam, Ph.D.

CONTRACTING ORGANIZATION:
Duke University
Durham, NC 27708

REPORT DATE:
October 2013

TYPE OF REPORT:
Annual

PREPARED FOR: U.S. Army Medical Research and Materiel Command
               Fort Detrick, Maryland 21702-5012

DISTRIBUTION STATEMENT:

    Approved for public release; distribution unlimited

REPORT DOCUMENTATION PAGE

Form Approved
OMB No. 0704-0188

1. REPORT DATE *(DD-MM-YYYY)* October 2013	2. REPORT TYPE Annual	3. DATES COVERED *(From - To)* 18 Sep 2012 – 17 Sep 2013

4. TITLE AND SUBTITLE	5a. CONTRACT NUMBER
Harnessing the power of light to see and treat breast cancer.	5b. GRANT NUMBER W81XWH-09-1-0410
	5c. PROGRAM ELEMENT NUMBER

6. AUTHOR(S)	5d. PROJECT NUMBER
Nirmala Ramanujam, Ph.D.	5e. TASK NUMBER
Go ckn[,]pko o kB f wng@gf w	5f. WORK UNIT NUMBER

7. PERFORMING ORGANIZATION NAME(S) AND ADDRESS(ES)	8. PERFORMING ORGANIZATION REPORT NUMBER
Duke University Biomedical Engineering 136 Hudson Hall; Box 90281 Durham, NC 27708	

9. SPONSORING / MONITORING AGENCY NAME(S) AND ADDRESS(ES)	10. SPONSOR/MONITOR'S ACRONYM(S)
U.S. Army Medical Research And Material Command	
Fort Detrick, Maryland 21702-5012	11. SPONSOR/MONITOR'S REPORT NUMBER(S)

12. DISTRIBUTION / AVAILABILITY STATEMENT

Approved for public release; distribution unlimited.

13. SUPPLEMENTARY NOTES

14. ABSTRACT
Our objective is to exploit the wealth of physiological, metabolic, morphological and molecular sources of optical contrast to develop novel strategies that focus on two breast cancer applications: tumor margin assessment and prediction of response to neo-adjuvant therapy. The proposed aims of this grant are expected to result in three major contributions. The first has the most immediate impact. An optically based strategy that can quickly and non-destructively detect positive tumor margins will decrease the need for re-excision surgery and thereby decrease the local recurrence rate and rate of distant metastases in women electing BCS. Gaining insight into the physiological, metabolic, morphological and molecular sources of heterogeneity within and among tumors and how they are modulated by therapy, drug resistance and metastatic potential will directly benefit prognostication, prediction of outcome and planning of cancer therapies. With these tools, clinicians and clinical researchers can get a better understanding of this disease and how it might react to a drug. Basic science researchers could use it as an informed approach to study tumor biology and assay the effect of novel therapeutic agents *in vivo*.

15. SUBJECT TERMS
optical spectroscopy, imaging, fiber-optic, molecular, screening, breast cancer

16. SECURITY CLASSIFICATION OF:			17. LIMITATION OF ABSTRACT	18. NUMBER OF PAGES	19a. NAME OF RESPONSIBLE PERSON USAMRMC
a. REPORT U	b. ABSTRACT U	c. THIS PAGE U	UU	59	19b. TELEPHONE NUMBER *(include area code)*

Standard Form 298 (Rev. 8-98)
Prescribed by ANSI Std. Z39.18

Table of Contents

1. INTRODUCTION:

Our objective is to exploit the wealth of physiological, metabolic, morphological and molecular sources of optical contrast to develop novel strategies that focus on two breast cancer applications: tumor margin assessment and prediction of response to neo-adjuvant therapy. The proposed aims of this grant are expected to result in three major contributions. The first has the most immediate impact. An optically-based strategy that can quickly and non-destructively detect positive tumor margins will decrease the need for re-excision surgery and thereby decrease the local recurrence rate and rate of distant metastases in women electing BCS. Gaining insight into the physiological, metabolic, morphological and molecular sources of heterogeneity within and among tumors and how they are modulated by therapy, drug resistance and metastatic potential will directly benefit prognostication, prediction of outcome and planning of cancer therapies. With these tools, clinicians and clinical researchers can get a better understanding of this disease and how it might react to a drug. Basic science researchers could use it as an informed approach to study tumor biology and assay the effect of novel therapeutic agents *in vivo*.

a. Original Statement of Work for 5 Years

Aim 1: Optical imaging of margin morphology on breast lumpectomy specimens: To evaluate the role of wide-field imaging (coverage) and high-resolution interrogation (localization) of breast margin morphology to guide surgical resection intra-operatively and pathologic assessment of the tumor margin post-operatively (Timeframe: year 1-5).

  1a. Development of one optical spectral imaging system that integrates sensing capabilities for aims 1 and 2 and a high-resolution probe that can image absorption, scattering and fluorescence contrast (timeframe, year 1).
  1b. Conduct clinical studies on lumpectomy margins on 200 patients (time frame, years 2-4)
  1c. Data analysis and interpretation (timeframe, years 3-5)
    Test the sensitivity and specificity of wide-field imaging to detect positive tumor margins
    Test sensitivity and specificity of high-resolution probe to detect IDC and DCIS.

Aim 2: Optical quantitative biology of different sub-types of breast cancer: To investigate biomarkers of oxygenation, carotenoids (β-carotene) and ECM proteins (collagen) in human breast cancer stratified by tumor sub-type and receptor status and their association with neo-adjuvant chemotherapy response.

  2a. Development of rotating needle compatible spectroscopy probe (timeframe, year 1).
  2b.Conduct clinical studies to measure optical biomarkers *in vivo* in 150 patients undergoing surgery (timeframe, years 2-4).
  2c. Conduct clinical studies to measure optical biomarkers from 75 patients before neo-adjuvant therapy
  2d. Data analysis and interpretation (years 3-5):
    Determine association of biomarkers with tumor subtype
    Determine association of biomarkers with receptor status

Determine association of biomarkers with genomic signatures

Determine association of biomarkers with pathologic sub-total and complete response

Aim 3: Optical quantitative biology to assess therapy response in different sub-types of breast cancer: To investigate biomarkers of oxygenation and ECM proteins (collagen and $\alpha_v\beta_3$ expression) in rodent breast cancer stratified by tumor sub-type, receptor status and metastatic potential in response to targeted and chemotherapies.

3a. To determine if multi-parametric intra-vital optical microscopy, measuring hemoglobin saturation, total hemoglobin, redox ratio, collagen, and integrin expression can monitor tumor response to tamoxifen in parental and tamoxifen-resistant MCF-7 tumors in the mouse dorsal skin fold window chamber (timeframe, years 1-2).
   - A total of 40 athymic nude mice will be required for this study (10 mice/group).

3b. Monitor optical parameters in the dorsal skin fold window chamber in response to doxorubicin chemotherapy in MCF-7 parental and doxorubicin-resistant tumors (timeframe, years 2-3).
   - A total of 40 athymic nude mice will be required for this study.

3c. Monitor optical parameters in the dorsal skin fold window chamber in response to doxorubicin chemotherapy in tumors that express high (MDA-435) and low (MCF-7) levels of $\alpha_v\beta_3$ integrin (timeframe, years 3-4).
   - A total of 40 athymic nude mice will be required for this study.

3d. Data and statistical analysis (timeframe, year 5).

Aim 3 has been slightly revised. The revised Aim 3 is titled, "*Optical imaging of tumor metabolism to predict long-term fate.*" See page 24 within the Body for details.

2. BODY:

Aim 1: Optical imaging of margin morphology on breast lumpectomy specimens

In Aim 1, our objective is to develop a strategy for high resolution fluorescence imaging of tumor margins, and to combine that with wide-field diffuse spectral imaging in a complementary fashion. For the high resolution fluorescence imaging component of the project, two years ago we demonstrated that preliminary application of sparse decomposition to high resolution images of acriflavine stained tissue shows promise for isolating individual tissue types and ultimately could allow for the automated detection of residual disease of surgical margins (see Aim 2 for additional information on high resolution imaging and development of the sparse decomposition algorithm). Additionally, we showed that both radiographic breast density and neoadjuvant status impact the spectroscopic data of the surgical margins and needs to be taken into account when diagnosing surgical margin status. Last year we focused on advancing optical imaging for breast margin assessment by analyzing excisional time, cautery and patent blue dye on underlying sources of contrast in patients undergoing breast conserving surgery. Here we

present the implementation of the 49-channel device which enables acquisition of wide-field images of the tumor margins in a shorter amount of time. We have made improvements to the system, including the implementation of pressure-sensing and raster-scanning techniques to minimize user-specific error, reduce false positives from margin compression during measurements, and improve resolution. These improvements are discussed in detail below.

Introduction:

We have previously demonstrated that wide-field optical imaging of tumor morphology detects positive margins (margins with IDC and DCIS) with accuracies that well exceed that of the breast surgeon. Here we prospectively validate the wide-field imaging system that we have developed and further refine our understanding of the micro-architectural differences between different types of tumor margin sub-types, in particular, DCIS, towards improving sensitivity and specificity. Our approach is to image the boundaries of the excised tumor mass, which is consistent with the existing paradigm for post-operative pathologic margin assessment, using the 49-channel device to acquire wide-field images of the tumor margins. We showed that both radiographic breast density and neoadjuvant status impact the spectroscopic data of the surgical margins and needs to be taken into account when diagnosing surgical margin status. We investigated the various sources of error on the optical properties of normal tissue and how these changes impact the accuracy of our predictive models. We are characterizing the performance metrics of the 49-channel system and are continuing to recruit patients for the imaging protocol. These results are described in more detail below.

Part A - Advancing optical imaging for breast margin assessment: an analysis of potential sources of error (excisional time, cautery, and patent blue dye) on underlying sources of optical contrast

Breast conserving surgery (BCS) is a recommended treatment for early-stage breast cancer and for breast cancers that have been reduced in size by neoadjuvant therapy. The goal of BCS is to excise the tumor along with a margin of normal tissue, while preserving as much of the normal breast tissue as possible. Unfortunately, as many as 18-72% of patients undergoing BCS require repeat surgeries due to a close or positive surgical margin diagnosed post-operatively and thus, require a re-excision surgery to achieve cancer free margins [1-9]. The large variation in re-excisions is thought to be due to differences in surgeon's training, in the definition of a close margin, and in the perceived risk of focally positive margins versus extensive involvement [10].

Surgery to remove the cancer and obtain clear margins is a collaborative effort between the surgeon and the pathologist (and in some institutions, the radiologist). In spite of this, there can be substantial variability in the prediction of positive margins in the intra-operative and post-operative settings. Surgeons do not have adequate intra-operative assessment tools to ensure that the cancer has been completely removed at the time of first surgery. Pathologists do not have adequate tools for sampling from areas on large tumor margins. The lack of these capabilities represents a significant unmet clinical need for margin assessment for both the surgeon and pathologist.

Optical imaging of tissue is an attractive solution to this problem because it is relatively fast and non-destructive. Optical techniques can also measure features related to the histological landscape without the need for labels. Before this technology can be used in an intra-operative setting or in a post-operative setting, systematic studies have to be performed to determine which surgical and post-surgical factors affect the precision and accuracy with which this technology maps optical contrast. This is true not only for our technology but other technologies, both optical and non-optical that are intended for this application. Specifically, if the technology is to be used on the excised margin (which is the way in which intra-operative pathology is performed), then there must be an understanding of how the presence of the blue sentinel lymph node mapping dye (referred to as patent blue dye) and cautery could influence the primary sources of contrast in the breast. Another important variable to characterize is the impact of the time delay after excision on the primary sources of optical contrast in the breast.

In this study, we examine the effects of time after excision on the following quantitative optical parameters in breast tumor margins which include: [β-carotene], oxygenated and deoxygenated hemoglobin, total hemoglobin concentration ([THb]), the wavelength-averaged reduced scattering coefficient from 450-600nm ($<\mu_s'>$), [β-carotene]/$<\mu_s'>$, [THb]/$<\mu_s'>$, hemoglobin saturation (HbSat), and patent blue dye. In addition, we evaluate the effects of varying and patent blue dye concentration and cautery on the optical absorbers and scatterers. Finally, we evaluated how all of these results impact optical contrast between negative and close/positive margins for the purposes of breast tumor margin assessment.

Methods:
Details of the analysis of the diffuse reflectance data from the partial mastectomy specimens can be found in prior publications [11-14] and were discussed in previous reports. Spectra were corrected for daily variations in optical throughput using a Spectralon reflectance standard, and were normalized by the CCD integration time. An inverse Monte Carlo model [11, 15, 16] was used to obtain values for THb concentration, β-carotene concentration and the wavelength-averaged reduced scattering coefficient from 450-600 nm ($<\mu_s'>$), for each measured site (or pixel) on the specimen surface. Upon completion of the measurements, the measured sites were inked for histological correlation. The specimens were then transferred to the surgical pathology laboratory for routine pathologic processing, and following routine diagnostic workup the inked sites were evaluated microscopically by the study pathologist. The benign sites were classified as fat, fibro-adipose, fibro-glandular, or mixed/other; mixed/other refers to any site with some combination of fat, collagen, glands, or vessels. The malignant sites were classified as invasive ductal carcinoma (IDC), ductal carcinoma *in situ* (DCIS), or mixed/other; for these, mixed/other refers to sites with some combination of IDC, DCIS, or lobular carcinoma. If tumor cells extended to the inked surface, the margin was considered positive. If they were within 2 mm of the inked surface, the margin was considered close.

Previously, the extracted tissue parameters were fit to a longitudinal mixed-effects model, which is an appropriate method for evaluating the trends over time in optical measurements across different tissue types. Longitudinal models were performed in R version 2.7.2 (www.r-project.org) using the lme4 package. The fixed-effect terms in the models were the time from surgical excision of the specimen and the histological subtype of the measured site. This model

resulted in a fitted slope for every measured site. In all tests of main effects and interactions, statistical significance was considered to be $p < 0.05$.

From April 2013 to present, lumpectomies were analyzed from 22 patients, 11 of which we have received site-level pathology on, resulting in 81 sites. From March 2011 to September 2011, lumpectomies were analyzed from 10 patients resulting in 80 sites. A total of 7 sites were excluded due to poor probe-tissue contact. The tissue was submitted for histopathology on the remaining 73 sites. However, histopathology could only be obtained for 61 of the sites. From May 2009 to October 2010, mastectomies from 19 patients were analyzed, resulting in 38 individually-measured tissue sites. The optical parameters were plotted versus time for every site and inspected for trends; 4 sites were removed due to poor probe-tissue contact and/or motion artifacts observed in the data, 2 additional sites (1 patient) were removed because the optical measurements were made 85 minutes after excision which was much longer than the other sites. Of the remaining 32 sites, 20 had microscopic histological confirmation. Samples with histology confirmation were given an overall diagnosis of benign or malignant, and were then given a further classification by specific histological subtype.

Results:
We previously determined that HbSat cannot be fit with a linear model due to excessive changes in oxygenated and deoxygenated hemoglobin post-excision. This is likely due to oxygen being consumed by the metabolically active tissue immediately after excision. Although HbSat may be a useful *in vivo* parameter for determining tumor hypoxia, or for examining the local microenvironment*,* or even for margin assessment of the resected cavity*,* it is not reliable in *ex vivo* margin assessment of breast tissue specimens. The results from both the simulated and phantom data for [patent blue dye] indicate that [patent blue dye] up to 80µM does not impact the extractions of [THb], [β-carotene], or $<\mu_s'>$ from the diffuse reflectance spectra; again, the highest concentration of patent blue dye seen in the previous lumpectomy study was 72.7µM. Although the errors were higher in the phantom data (as would be expected), there was no trend in the percent error with increasing [patent blue dye]. In terms of tissue cauterization, we found that initial measurements of [THb] were significantly higher in the benign sites of the cauterized lumpectomies compared to the mastectomies. This initial difference could be due either to varying excisional times for mastectomy and lumpectomy procedures or due to cauterization. Since we observed no significant correlation between the initial value and time from excision, we assume that this difference in [THb] is due to cauterization of the vasculature to prevent blood from draining out of the vessels as rapidly as it would in mastectomy specimens. For all tissue parameters, the rate of change was not significantly different between the benign and malignant sites. This is an important finding for margin assessment which indicates that optical contrast between benign and malignant regions of a margin will be preserved, regardless of the time when the margin is imaged over a 30 minute window. We also showed that there was no correlation between the time from excision and the initial value (or first measurement) of the optical data. This suggests minimal change in the data within the time window that we examined (17 ± 4 minutes post-excision and measured for 10-32 minutes). Additionally since there was no significant difference between the lumpectomies and mastectomies for [β-carotene] and [β-carotene]/$<\mu_s'>$, we can extrapolate these findings to benign and malignant tissue in cauterized lumpectomies.

Part B - Clinical Study on Margin Assessment: higher resolution, coverage, and controlled pressure sensing in evaluating lumpectomy specimens

It has been determined that on average 1.5 margins per patient will present with a positive margin upon pathological review based on a statistical analysis by our collaborating statistician. Since these positive margins are usually due to small, focal positive regions on the margin, it is imperative to optically assay the entire margin in order to ensure that these small cancer-positive regions are detected. To that end, we have designed and constructed multiplexed probes for the study; generation three contains 49 channels (Figure 1.1). These changes have required modification to the probe design, and minor modification of the optical instrument.

The ability to acquire data from 49 sites simultaneously will allow us to optically assay a much more significant area of the tissue specimen. The system design has been further improved with the fabrication of an imaging platform that enables the implementation of new techniques: raster scanning and pressure sensing (Figure 1.2). The goal of these improvements is to minimize user-specific error, reduce false positives from margin compression during measurements, and improve resolution.
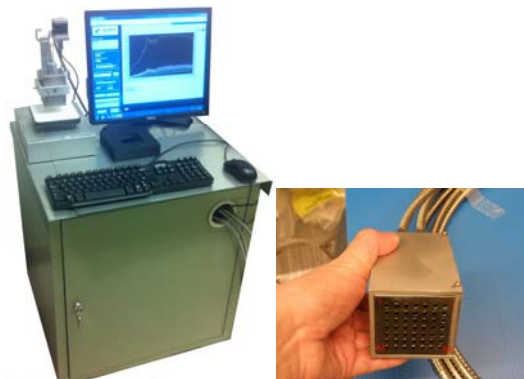
Figure 1.1: Image of 49-Channel System and probe with 49 channels.

Figure 1.2: Image of the translation stage that automates raster-scanning and pressure-sensing.

Methods:

System design

The 49-Channel system consists of a 300W xenon lamp, a house-made optical switch, a custom built 49-ch imaging probe, and an Andor Shamrock spectrograph with a 512x512 CCD camera (Figure 1.3). At the common end, the 49 channels are arranged into a 7x7 array, covering an area of 4.2x4.2 cm^2. Each probe has a single 200μm fiber for light detection surrounded by a ring of eight 200μm fibers for illumination with a source-detector separation of 600μm. The 49 pixels are divided into two sets: the odd (red) set and even (blue) set. The red and blue pixels are turned on and off sequentially using the optical switch. All the detection fibers are arranged as a linear array in order in the spectrograph adaptor. By dividing the pixels into two sets, we doubled the number of channels that can be imaged because no inactive fibers are required for spacing on the CCD.

A calibration channel was also added into each set for real-time instrument calibration. Therefore there are a total of 51 fibers in the collection fiber bundle. The maximal number of channels that can be imaged is limited by the fiber diameter, CCD chip size and magnification of the spectrograph. In this system this number is 51x200/220 um bare fibers.
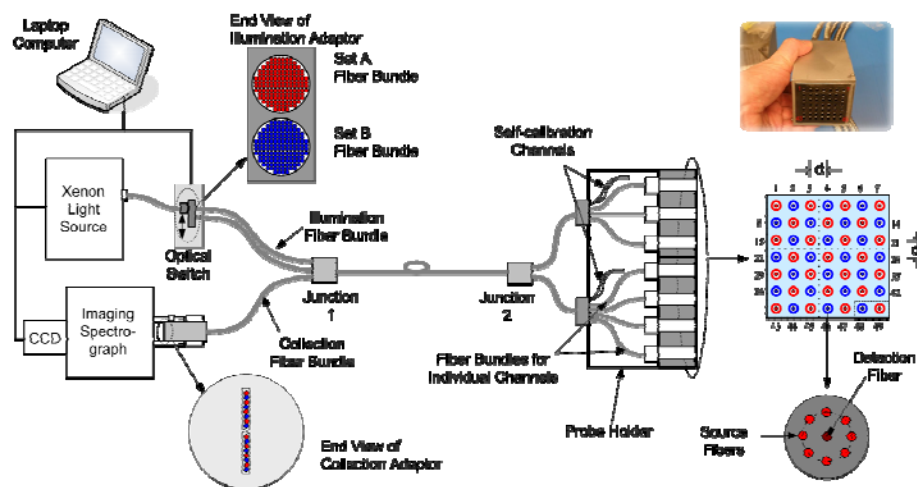

Figure 1.3: Schematic of the 49-Channel System.

Clinical study design

Duke University Health System performs approximately 150-200 partial mastectomies annually. Intra operative margin assessment using the optical assay system will be carried out on 400 patients undergoing partial mastectomies, mastectomies or reduction mammoplasties. This is a sufficient sample size for the purpose of determining the sensitivity and specificity of the optical assay system. After these specimens are evaluated with the optical assay apparatus, they will be submitted for routine pathology by Dr. Joseph Geradts.

In order to increase the chances of measuring a positive area on the tumor, we will measure all sites on two margins that the surgeon identifies as most likely positive for each specimen (up to 200 sites depending on specimen size). This methodology gives us the best chance to detect positive regions on the tissue specimens without altering the clinical design. We will employ a real-time spectral analysis algorithm to determine which 10 of the measured sites are most likely to be positive for tumor (as opposed to the random sampling); these sites will be subsequently inked for pathologic review.

Results:

We are now characterizing the performance metrics of the 49-channel system and comparing it to the clinical criteria for intra-operative tumor margin assessment. These metrics include SNR, sensing depth, cross-talk, reproducibility, resolution, speed, drift, phantom study accuracy, and channel uniformity. These results are summarized in Table 1.1. All of these performance metrics are being tested on phantoms, and a subset is being tested with clinical data (reproducibility and resolution).

Table 1.1: Main system characteristics of the 49-channel system.

System characteristic	49 CH
Coverage per scan (cm^2)	17
Sensing depth (mm)	0.8-2.5
Mean SNR (dB)	44.6
Cross-talk on the CCD (%)	*Separating channels into 2 sets: < 1*
Tissue cross-talk (%)	2.4

Device improvements

The system design has been further improved with the fabrication of an imaging platform that enables the implementation of new techniques: raster scanning and pressure sensing. The custom pressure-sensitive imaging platform allows the user to control the pressures that are maintained at the specimen to probe interface. Raster scanning allows for increased resolution by scanning interleaving spaces. LabVIEW software automates the acquisition such that user-specific error is eliminated with the motorized stage that applies pressure and performs raster-scanning. There is a trade-off between time for raster scanning and the amount of time allotted to measure in the clinic. This trade-off between time and raster scanning is illustrated in Figure 1.4. These additions to the 49-channel system have been tested clinically on a cohort of 26 patients undergoing lumpectomy and reduction mammoplasty surgeries.
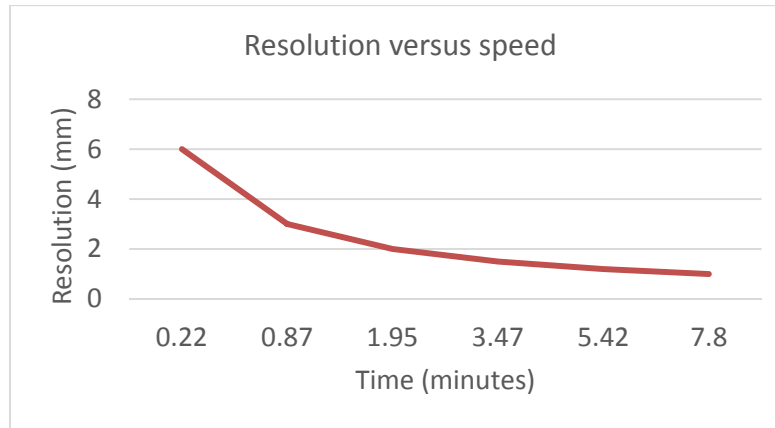
Figure 1.4: Illustration of the trade-off between improved resolution and time for measurement.

Clinical data

From April 2013 to present, we acquired images using the 49-channel system with raster-scanning and pressure-sensing improvements in 26 patients undergoing partial mastectomy or reduction mammoplasty. Last year, we acquired images using the 49-channel system in 54 patients undergoing partial mastectomy, mastectomy or reduction mammoplasty. Of these samples, 29 have been imaged by the high resolution microendoscope. The goal of this imaging protocol was to use wide field spectral imaging of the entire margin followed by high resolution fluorescence interrogation of optically identified suspicious sites. This year we have begun using a more reliable form of calibration by taking a puck measurement instead of the use of self-calibration and have achieved higher resolution with the technique of raster-scanning, eliminating the need for the use of the high resolution microendoscope.

Software has been developed to invert the diffuse reflectance spectra from the 49-channel system and create optical parameter maps corresponding to the probe geometry using the previously detailed Monte Carlo inversion algorithm [11, 15, 16] (with the Mie model for scattering). The software uses both the diffuse reflectance data and the model fits to process the images, discarding any pixels that were not in contact with tissue or resulted in poor fitting. To date, we have acquired images using the 49-channel system in 26 patients undergoing partial mastectomy or reduction mammoplasty. An example of an analyzed margin upsampled with a factor of 5 (1.2mm resolution) can be found in Figure 1.5. This sample image was of a small specimen located under the bottom left corner of the 49-channel probe.
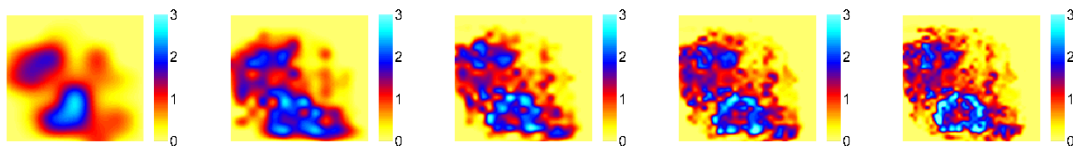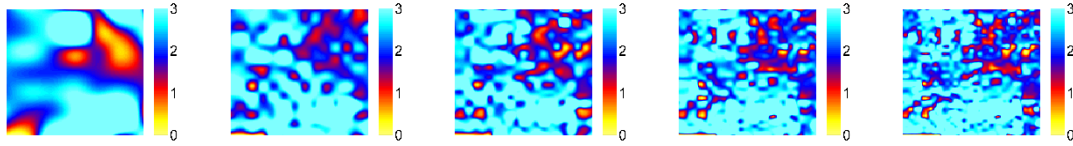
Figure 1.5: Five sequentially downsampled images of β-carotene to scattering in a close margin (top row) versus a negative margin (bottom row).

Plans for year 5:

In year 5, we will continue recruiting patients for the imaging protocol and determine the accuracy of the 49-channel system in detecting positive margins. With this improved 49-channel system with pressure-sensing and raster-scanning capabilities, we will study the use of optical endpoints to determine clinical outcome.

Aim 2: Optical quantitative biology of different breast cancer subtypes

Part A – Duke University

The objective of the work in Aim 2 is to use optical techniques to measure markers of the tumor microenvironment in women with cancers representing a wide variety of subtypes, and to determine whether these optical measures can be used for real time diagnosis or to predict eventual chemotherapy response in a subset of the patients who are measured prior to commencement of chemotherapy. One such approach that we have discussed in previous years is to use a high resolution microendoscope (HRME) combined with a morphological stain called acriflavine to visualize the tissue morphology in real time. In previous years we demonstrated the feasibility of using the HRME for detection of residual carcinoma in the normal tissue milieu and validated our unique image analysis approach on preclinical murine tumor margin specimens and small cohort of clinical mastectomy samples. Last year, we completed a large study using the HRME to capture morphologically based information from biopsy specimens. Here we focus primarily on our quantitative approach for diagnosing HRME images of heterogeneous breast tissue acquired from biopsy specimens. In Year 4, we continued to image biopsy specimens, have identified several quantitative endpoints to distinguish malignant from benign tissues, and have laid the groundwork to build a diagnostic classification model.

Optical microscopy is a powerful technique to obtain high-resolution images of tissue histology in real-time at the point-of-care, without the need for fixing, sectioning, and staining. Various optical microscopy techniques including reflectance and fluorescence[12, 17, 18], Raman[19], confocal[20, 21], and optical coherence tomography[22, 23] have been used to exploit intrinsic sources of contrast in thick tissues. Additionally, fluorescence microscopy has been combined with vital fluorescent stains such as acridine orange (AO)[24-26], acriflavine[27, 28], and DAPI[29] to visualize micro-anatomical features in skin[24], breast[29], ovarian[26], oral[27], and esophageal[28] cancers. All of these technologies enable rapid and completely non-destructive visualization of tissue histology.

While optical microscopy is well suited to enable visualization of tissue morphology at the point of care, robust methods for segmentation and quantitative analysis are essential to enable

automated diagnosis. Thus, the goal of this work is to maintain high resolution imaging of tissue morphology through employing fluorescence microscopy and vital fluorescent stains but to also develop a quantitative strategy to segment and quantify tissue features, such as nuclei and the surrounding tissue, which will enable automated diagnosis of thick tissues.

There are three important criteria that have to be considered in the selection of an appropriate image analysis strategy. (1) If the background patterns and intensities vary greatly between images (i.e. if images are heterogeneous), will a method still be able to isolate features of interest, such as tumor nuclei? (2) Can the method resolve overlapping nuclei when attempting to characterize nuclear size or density? (3) Does the method require human intervention and supervision, thus introducing subjective bias and complexity into the analysis?

Many approaches for cell or cell nuclei segmentation exist. A summary of the advantages and disadvantages of commonly used approaches for nuclei segmentation in microscopy is included in Table 2.1. Global thresholding approaches work well when cell nuclei do not overlap and background intensities are evenly distributed, and its use in isolating cell nuclei is well established in the literature [29-32]. However, it is also broadly recognized that global thresholding has many shortcomings, specifically that it has limited utility in heterogeneous images in which background intensities vary greatly. While global thresholding takes intensity information into account, it does not incorporate *geometric* information, such as the expected size or shape of nuclei. Thus, in an effort to take geometry into account, many groups have developed techniques that combine global and local image information, such as adaptive window thresholding or local maxima detection [30, 33-38], active contours [39-42], watershed segmentation [38, 43, 44], high pass filtering [45], and the circle transform [46]. In adaptive window thresholding or local maxima detection, regions or windows of the image are examined separately and the nuclei within each region are identified based on intensity information through either finding maximum intensities or applying a threshold [30, 33-38]. For heterogeneous images, the window size and threshold within each window should ideally vary across images and patients in order to effectively segment nuclei which are surrounded by various structures, such as muscle, adipose tissue, or other types of connective tissue. Tuning so many parameters on an image by image basis quickly can become unmanageable and introduce subjective bias into the quantification of nuclear size and density. Active contours, such as snakes, find the boundary of a feature by minimizing an "energy" function associated with the current contour that measures the contour's curvature and enclosed area [39-42]. However, choosing or defining the energy function can be a complex process, and segmentation results are highly sensitive to this choice. Additionally, active contours require human intervention and supervision through manually guiding the outlining of features or selecting a pixel in the interior of each structure (e.g. tumor nucleus) to be extracted. In images that contain large collections of nuclei, this segmentation approach can quickly become unwieldy. Furthermore, due to the complexity of this computational technique, it is difficult to know when an optimal solution has been achieved. In watershed segmentation methods, an image is partitioned into regions separated by watershed lines. While watershed segmentation can identify overlapping nuclei, it is vulnerable to a well-recognized phenomenon called over-segmentation, in which homogeneous regions are segmented into multiple different regions erroneously [38, 43, 44]. These effects can be somewhat mitigated via an involved parameter

tuning process requiring significant human intervention or through variations to the watershed transform, such as viscous watershed [47]; generally, this is an area of active ongoing research. Furthermore, there are many regions in an image that are segmented via watershed methods that are not meaningful for our purpose of isolating nuclei within heterogeneous images. For example in heterogeneous images, the improper segmentation of background elements such as adipose or connective tissue can mistakenly be identified as nuclei, leading to incorrect quantitation of nuclear size and density. High pass filtering is a technique that is commonly used to isolate edges in images, and can be used to segment small features such as nuclei [45]. While high pass filtering is simple to implement and easy to tune, it is highly sensitive to noise present in an image. Lastly, the circle transform can be used to detect approximately circular objects of a specified range of radii within an image [46]. While this technique is simple and can identify overlapping nuclei, it assumes that objects are approximately circular and is sensitive to small variation in background intensity. Because of this sensitivity to small variations in the background, the circle transform, in isolation, is a suboptimal approach for heterogeneous images.

Table 2.1. Nuclei segmentation methods

Method	Advantages	Disadvantages
Global thresholding	Simple, easy to tune	Requires uniform background intensity
Adaptive thresholding	Simple	Requires varying window size across image and adjusting threshold within each window
Active contours	Can find object outlines in complex images	Requires defining complex energy function and human intervention and supervision
Watershed segmentation	Can identify overlapping nuclei	Results in over segmentation
High pass filter	Simple, easy to tune	Sensitive to noise
Circle transform	Simple, can identify overlapping nuclei	Sensitive to small variations in background intensity

Despite the diversity of approaches, segmentation of cells and cell nuclei remains a challenge due to the complexity of images that have varying levels of contrast and non-uniform background heterogeneity, as well as overlapping nuclear features. To address this important need, we have developed a computational technique that leverages morphologic information inherent in monochrome images of fluorescently-stained microanatomy to separate and quantify the presence of distinct tissue types in a heterogeneous image. First, sparse decomposition

(SD) [48] is used to separate cell nuclei, fibrous components, and adipose components. Second, a thresholding algorithm (TH) is applied to the deconstructed image to quantify the nuclear size and density as a means to identify the presence of disease in a breast biopsy specimen. While the TH is sensitive to small variation in the background, this effect is mitigated by first using SD to remove the background. This aim describes a methodology that systematically evaluates the potential of an image processing approach or combination of approaches, for a specific biomedical problem. The image processing approach chosen here is SD followed by TH, and the specific indication is the ability to isolate nuclei from heterogeneous breast biopsy images. The rationale for selecting SD is that it can segment different types of structures (nuclei, fibrous tissue, and adipose tissue) in complex heterogeneous images. TH was chosen to isolate nuclei because it can quickly be used to calculate nuclear size and density and is easy to tune. It should be noted that the combination of SD+TH is not the only solution to this complex problem; however, it is a well-justified approach to analyzing images from heterogeneous tissues and certainly could be adapted to include other methods if they can benefit the overall approach. Unlike image processing techniques which rely solely on intensity information (and are thus susceptible to calibration errors), SD incorporates geometric information through the property of sparsity. This leads to a highly flexible approach that requires tuning a very small number of parameters, can resolve overlapping nuclei, and does not require human intervention or supervision. Additionally, this technique does not discard image content but rather retains all of the image information inherent in the image to preserve spatial relationships between tissue types, which are essential for proper interpretation of the images.

Methods:

Imaging system and contrast agent: A fluorescence microendoscope device that has previously been described in detail [27] was used to collect images of acriflavine stained tissues. The system contained a 455 nm light emitting diode (Luxeon V Star, LXHL-LR5C), excitation filter (Semrock, FF01-452/45-25) dichroic mirror (Chroma 485 DCLP), emission filter (Semrock, FF01-550/88-25), CCD camera (Point Grey Research, GRAS-14S5), and coherent fiber bundle (Sumitomo, IGN-08/30). The fiber bundle was composed of 30,000 fibers giving a circular field of view of approximately 750 µm in diameter. The resolution of the system was 4.4 µm. Images were produced by placing the fiber bundle in contact with the acriflavine stained tissue surface. Acriflavine (0.01% w/v, Sigma-Aldrich) dissolved in phosphate buffered saline (PBS) was topically applied to all specimens immediately prior to imaging.

Imaging protocol: Patients undergoing a biopsy procedure at Duke University were consented. After the biopsy was removed from the patient, acriflavine was applied to the surface of the specimen. The distal end of the HRME fiber bundle was placed in contact with the tissue and images were acquired. The biopsy was scanned length-wise by systematically moving the probe in 1 mm increments over the tissue surface. Once one side was scanned, the biopsy was rotated 180 degrees and the length-wise scanning process was repeated. In order to improve the accuracy and reproducibility of these movements the fiber bundle was secured in a custom probe holder fiber chuck which was mounted on an x-y translation stage. Between each probe placement the distal end of the probe was cleaned with 55% ethanol.

Pathologic co-registration: After the imaging session the surface of the specimen was inked for pathologic co-registration. In order to maintain the proper orientation of the specimen for pathological evaluation, each end was inked with a different color. After imaging and inking was complete, the tissue was returned for standard pathologic processing, and the resulting hematoxylin and eosin (H&E) stained slides were reviewed by an expert oncology pathologist who was blinded to the results of HRME imaging. A diagnosis for each end of the biopsy as well as a diagnosis for the middle portion of the biopsy was given.

Image analysis. Since the most clinically relevant goal is to detect the presence of microscopic disease, we focused our quantitative approach on first isolating features of interest, such as nuclei, and then calculating features that may be used to determine the presence of tumor cells in an image, such as the size and density of those nuclei. In order to isolate the cell nuclei from other structures, such as muscle fibers/fibrous tissue or adipocytes, tissue components (nuclei, muscle fibers/fibrous tissue, and the outline of adipose cells) were separated computationally using the SD method. SD has been used previously in the image processing community for image compression, enhancement, and restoration, but has never been applied to separate distinct tissue types in a heterogeneous image. The key assumption was that each tissue component has a different "sparsifying" dictionary in which the expansion coefficients were nearly all zero, with only a few large coefficients. (For instance, an image of muscle fibers was relatively smooth, so it could be accurately approximated using a superposition of a small number of Fourier basis functions.) If the sparsifying dictionaries were sufficiently dissimilar, then the sparsity could be exploited to uniquely identify the different tissue components. The pixel dictionary was used for the nuclei to capture the small and spatially isolated nuclei. The discrete cosine transform (DCT), a variant of the Fourier transform, dictionary was used to describe muscle or fibrous components with periodic fiber structures. Adipose tissue can be described as localized piecewise smooth features, and therefore curvelets are well suited to capture adipose features. Specifically, curvelets, which are similar to wavelets, have dictionary elements corresponding to different scales and locations throughout an image and is relatively dissimilar to both the pixel and DCT dictionaries [49]. An illustration of the sparse decomposition algorithm applied to image containing adipose cells with nuclei scattered throughout is shown in Figure 2.1. In this example the DCT image is black because there is no muscle or fibrous tissue present in the original image.
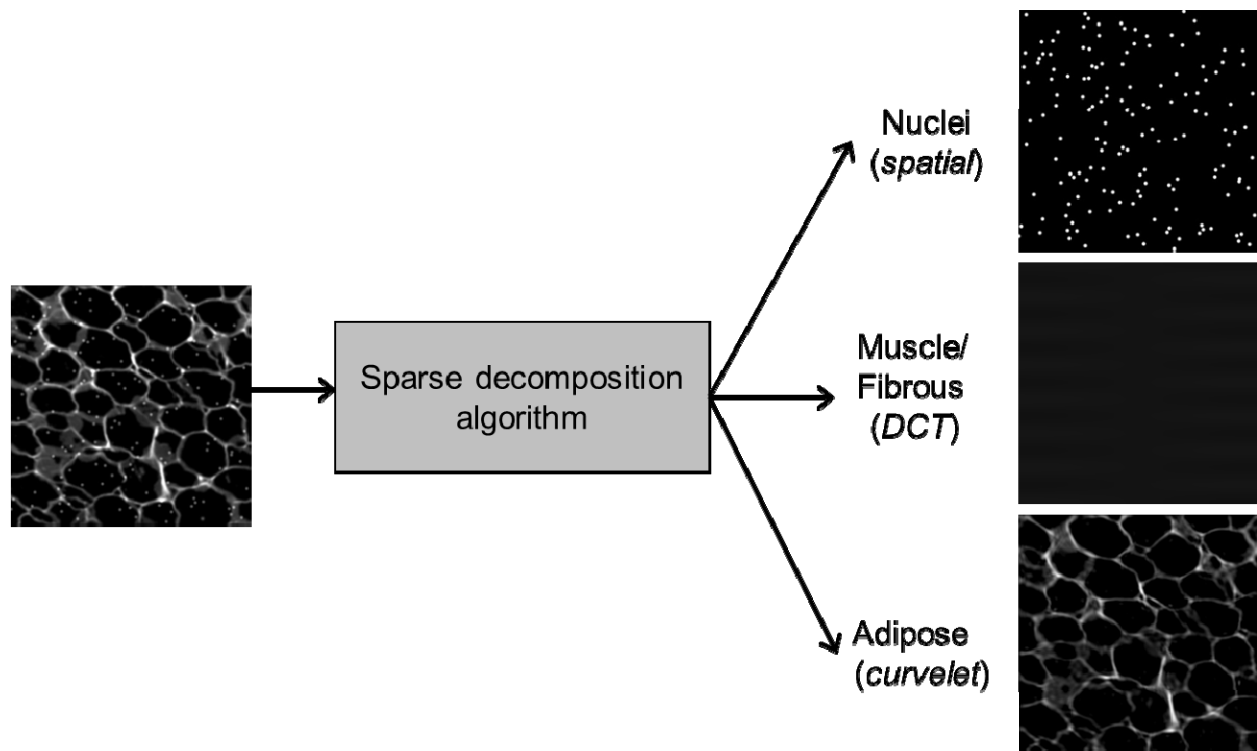
Figure 2.1: Sparse decomposition illustration. An image containing adipose cells with nuclei scattered throughout can be separated into its constituents through the sparse decomposition algorithm. The spatial image captures the randomly distributed nuclei, while the DCT image describes the periodic muscle components and the curvelet image captures the curved outline of adipose cells. In this example the DCT image is black because there is no muscle or fibrous tissue present in the original image.

Statistical analysis: In order to compare the ability of different variables (such as nuclear size and density) to distinguish between malignant and benign biopsies, receiver operating characteristic (ROC) curves and the area under the curve (AUC) were calculated using a web-based tool [50]. The Youden index, which is a frequently used summary measure for ROC curves, was calculated for each ROC curve, and the associated sensitivity and specificity is reported for each variable [51].
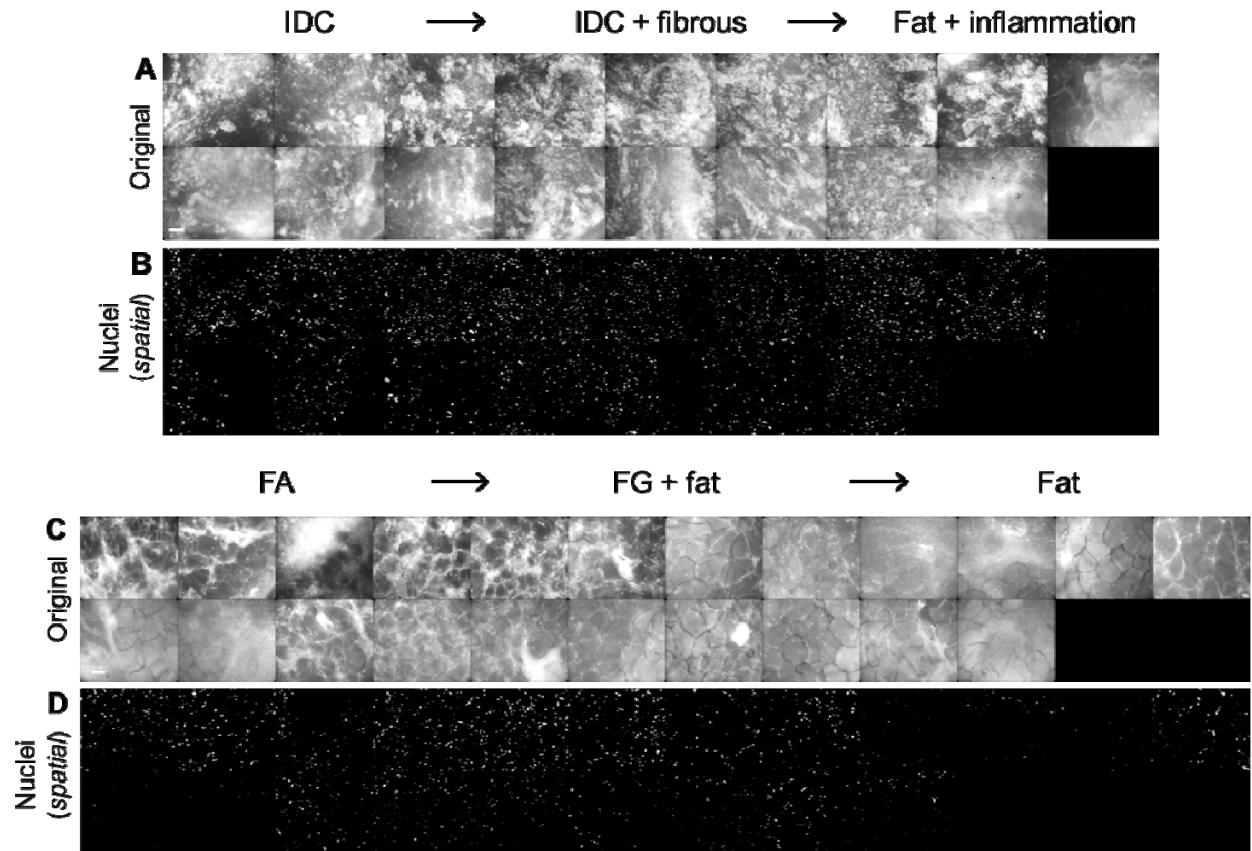
Results:

The breakdown of biopsies specimens imaged in this study is shown in Figure 2.2. We consented 56 patients and were able to image 50 biopsy specimens (we had 6 screen fails for various reasons). We currently have received a pathology diagnosis for 47 of the 50 (1 pathology report is pending at this time). Out of the 47 with pathology, 42 were ultrasound guided biopsies in which a solid mass is detected, and 5 were stereotactic biopsies in which micro-calcifications are present. For the rest of the analysis, we focus primarily on the ultrasound guided biopsies since they yield images with superior image contrast. Within the 42 ultrasound guided biopsies, we have 18 malignant and 24 benign specimens. The 18 malignant are comprised of 14 invasive ductal carcinomas (IDC), 2 invasive lobular carcinomas (ILC), 1 ductal carcinomas in situ (DCIS), and 1 that contains both IDC and DCIS. Of the 24 benign biopsies, 19 contain some combination of fibrous and fat tissue. The remaining 5 benign biopsies are either fibroadenomas, papillomas, fibrocystic change (FCC), or have other benign

pathologies, such as an organizing hematoma or benign lymph node.
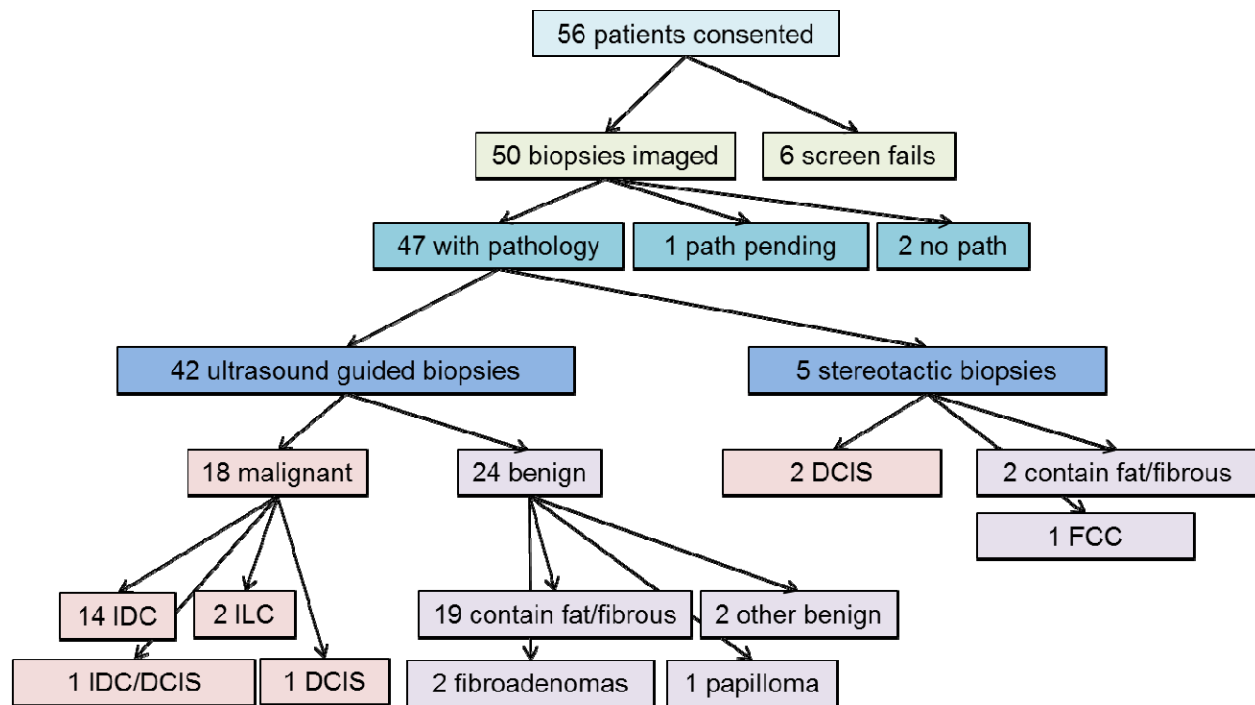
Figure 2.2: Breakdown of biopsy specimens.

Figure 2.3 shows a representative example of a malignant and benign biopsy from our study. As described in the methods each side was scanned length-wise—side 1 corresponds to the top row and side 2 corresponds to the bottom row. In the malignant example (A), the left hand side contains IDC, the middle contains IDC and fibrous tissue, and the right hand side contains fat tissue and inflammation. As seen, large round cells, characteristic of adipose tissue, can be seen on the right hand side, while the rest of the panel is filled with a random distribution of disorganized nuclei, which is characteristic of IDC. The corresponding nuclei (spatial) output from SD is shown in (B). As seen, many nuclei are present throughout the panel. In the benign example (C), the left hand side contains fibroadipose tissue (FA), the middle contains fibroglandular (FG) and fat tissue, and the right hand side contains fat tissue. As seen, large round cells interspersed with string-like fibrous tissue, characteristic of fibroadipose tissue, can be seen on the left hand side, while the middle and right hand side of the panel contains primarily adipose and less fibrous tissue. The corresponding nuclei (spatial) output from SD is shown in (D). As seen, nuclei that are primarily located on the periphery of the adipose cells are isolated throughout the panel.

Figure 2.3: Sparse decomposition (SD) applied to a representative malignant and benign biopsy. Both sides of the biopsy we scanned length-wise resulting in the two rows in (A) and (C). The pathological diagnosis for (A) was given for the left end (IDC), middle (IDC + fibrous tissue), and right end (Fat + inflammation) respectively. The pathological diagnosis for (C) was given for the left end (FA), middle (FG + fat tissue), and right end (Fat tissue) respectively. The nuclei (spatial) outputs from SD are shown in (B) and (D) respectively. Scale bar 100 μm.

After obtaining the nuclei outputs from SD, we sought to calculate parameters, such as the density and size of nuclei, which could have diagnostic potential. However, in order to ultimately diagnose the biopsy specimens, the variables calculated for each image within a mosaic need to be consolidated. For example, in the malignant biopsy shown in Figure 2.3 there are 17 images. If the nuclear density present in each image is quantified, then we have 17 density values (one for each image). In order to classification each biopsy as positive or negative, a summary statistic, such as the average nuclear density must be calculated. An outline of our quantitative procedure is shown in Figure 2.4.
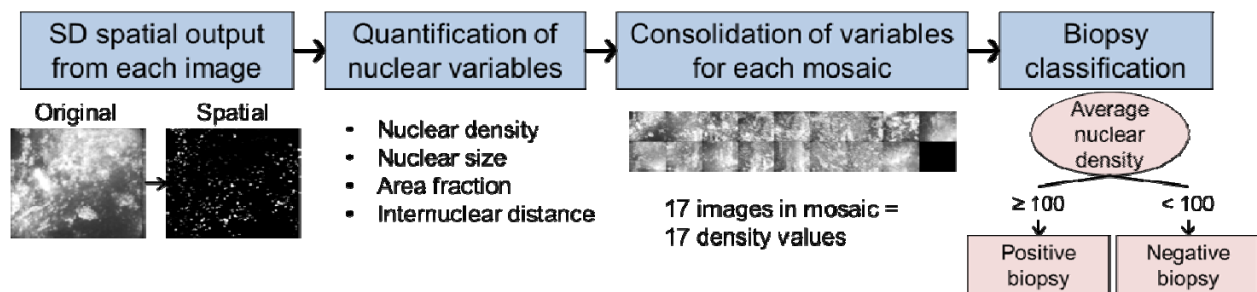
Figure 2.4: Outline of quantitative approach. After each image is put through SD, different variables are calculated that capture the nuclear morphology. However, variables must be consolidated such that each biopsy can be classified as positive or negative.

Thus far, we have calculated a host of nuclear variables for each image, each of which is illustrated in Figure 2.5. Variables include nuclear density (the number of nuclei in a unit area), area fraction (the total nuclear area divided by the total area), minimum internuclear distance (the distance from the nuclei center to the next closest nuclei center), and nuclear size (the diameter of each nucleus).
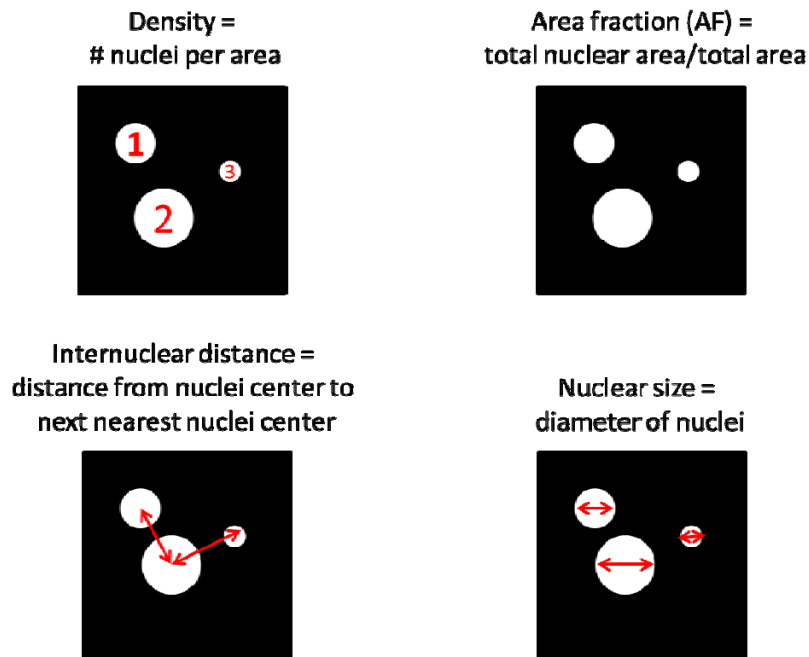
Figure 2.5: Illustration of nuclear variables.

When consolidating of variables, such as nuclear density, we want to be sensitive to spatial information, such as local increases in nuclear density, which is characteristic of focal disease. With this in mind, we have illustrated three different consolidation strategies in Figure 2.6. The first is to calculate the density present within each image. While this is the most straight-forward and obvious approach, it may wash out contrast between positive and negative specimens because it loses critical spatial information. Another approach is to calculate local increases in density via manual window selection. While this approach retains contrast, it requires that the user manually select the window size and location, which can quickly become unwieldy and introduce user bias into the analysis. The last approach is to overlay a grid onto each image and calculate the density present within each bin. While this approach requires grid size selection, it retains density contrast and captures critical spatial information. We have applied both the image density and grid density approach to the 18 malignant and 24 benign ultrasound-guided biopsies.

Image density	Localized density	Grid density
Washes out contrast and loses critical spatial information	Retains contrast but requires manual window selection	Retains contrast and spatial information but requires grid size selection
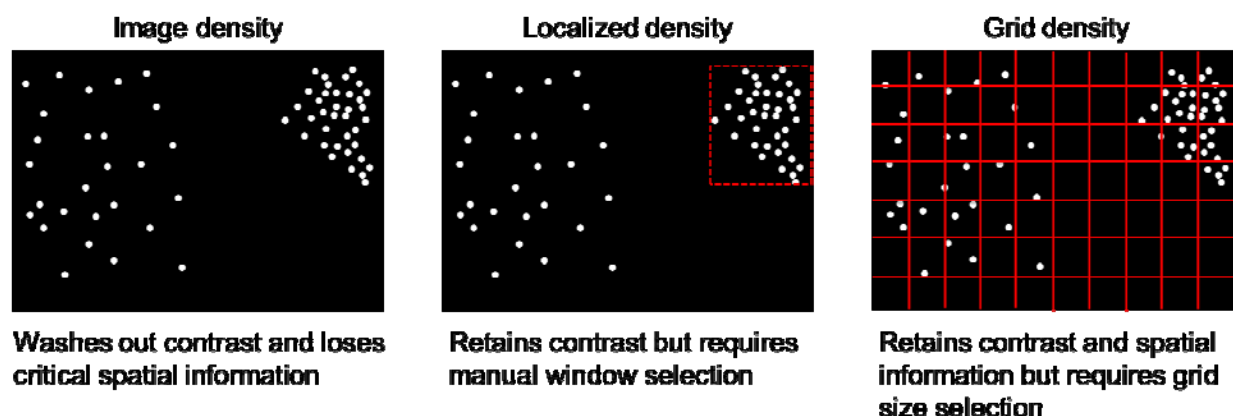
Figure 2.6: Different nuclear density consolidation strategies.

In order to compare the performance of the different variables and different consolidation strategies, we graphed receiver operating characteristic (ROC) curves and calculated the area under the curve (AUC). Additionally for each combination, the Youden index was calculated, which yields a sensitivity and specificity associated with the ROC. The top 20 performing variables are listed in Table 2.2. Column 1 indicates the rank associated with the AUC. Column 2 indicates the bin size in units of pixels. For this analysis, the bin size was varied from 10, 15, 20, 25, 50, 100, 200, to 606 pixels, which is the size of an entire image and which signifies that the image density consolidation method was used. Column 3 indicates one of the four variables that were calculated, which include density, area fraction (AF), minimum internuclear distance (Mindistance), and size. Column 4 indicates the summary statistic calculated to reduce each biopsy to a scalar value. Possible summary statistics include calculating the mean including the zero-valued bins/images (mean with 0s) or excluding the zero-valued bins/images (mean without 0s), calculating the percentage of bins greater than some threshold x (% bins>x), or calculating the quantiles of a variable, which is a point measure taken at intervals from a cumulative distribution function (CDF) of a random variable (for example 0.5 quantile is the median of the distribution). Column 5 contains the AUC associated with each combination. Columns 6 and 7 contain the sensitivity and specificity associated with the Youden index.

As seen, the Mindistance calculated on the image level (at a bin size = 606) with the bin percentage summary statistic yields the three highest AUCs. This is followed by density calculated on the image level with a mean without zeros summary statistic. Both density and Mindistance dominate the top 20 performing variables. AF is listed toward the bottom, and size does not appear in this table. This indicates that the density and Mindistance are the top performing variables for distinguishing positive from negative biopsy specimens.

Table 2.2: Performance of different variables

Ranking	Bin size (pixels)	Variable	Summary statistic	AUC	Sensitivity	Specificity
1	606	Mindistance	%bins<75	0.745	56	88

2	606	Mindistance	%bins<50	0.745	50	92
3	606	Mindistance	%bins<100	0.743	44	96
4	606	Density	Mean without 0s	0.736	56	88
5	10	Density	%bins>1	0.734	56	83
6	606	Mindistance	%bins<25	0.727	78	75
7	20	Density	%bins>2	0.725	72	71
8	25	Density	%bins>2.5	0.725	44	92
9	606	Density	0.5 quantile	0.725	56	92
10	15	Density	%bins>1.5	0.722	56	83
11	100	Density	Mean without 0s	0.720	78	63
12	200	Density	Mean without 0s	0.720	83	54
13	50	Density	%bins>3	0.718	44	92
14	200	Density	0.90 quantile	0.714	83	54
15	25	Density	Mean without 0s	0.704	67	79
16	10	Density	%bins>2	0.701	67	75
17	200	Density	0.95 quantile	0.700	83	58
18	606	AF	0.5 quantile	0.697	56	88
19	606	Density	0.75 quantile	0.696	61	75
20	200	Density	Mean with 0s	0.694	50	88

To further compare the different consolidation methods, ROCs of the best performing density variables were plotted and are shown in Figure 2.7. (A) shows the best density variables that were calculated using the image density consolidation strategy, while (B) shows the best density variables calculated using the grid density consolidation strategy. Lastly (C) shows the best performing Mindistance variables, which thus far have only been calculated with the image level consolidation strategy. All three plots yield comparable results with AUCs ranging from 0.696-0.745. This indicates that the grid density and image density consolidation strategies yield similar performance for distinguishing positive from negative biopsies; however, both approaches when used together in a classification model may together yield better optimal performance than when used in isolation.
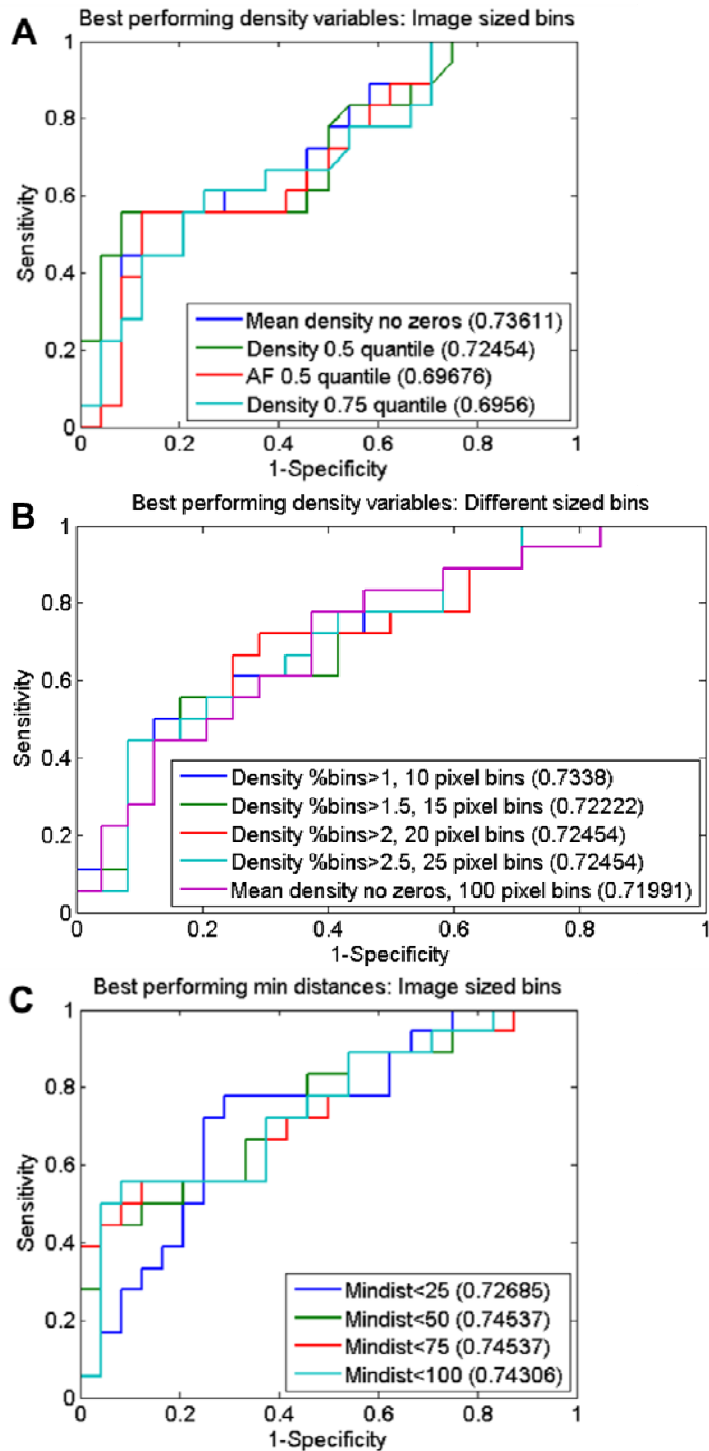
Figure 2.7: ROCs of different variables.

In conclusion, high resolution fluorescence imaging of acriflavine stained tissue combined with an algorithm that leverages sparse decomposition analysis provides a rapid, non-destructive and automated strategy for quantitative pathology of thick tissues with non-uniform background heterogeneity. Initial analysis of biopsy specimens with the grid density approach yields

comparable performance to the image density approach. This provides a powerful alternative to complicated and time-intensive immunohistochemistry techniques, which require fixing, sectioning, and staining and which can only be diagnosed by a highly trained pathologist.

Conclusions:
Preliminary results show that adipocyte area is lower when adjacent to some lesions of invasive ductal carcinoma than in normal tissue adjacent to collageneous tissue. The findings of this study indicate that adipocyte size could potentially be used as an architectural biomarker to characterize the malignant potential of a lesion. This information could potentially aid in selection of targeted chemotherapeutic agents. Additional work should be done to evaluate clinical factors and/or genetic/epigenetic factors that correlate with adipocyte size.

Plans for year 5:

During year 5, we plan to optimize our diagnostic model to yield the optimal separation between positive and negative biopsies. This includes identifying additional endpoints/parameters that have diagnostic potential, optimizing our consolidation strategy, and ultimately building predictive models that can quantitatively diagnose high resolution images in real time. Together, this work will yield an optimized set of tools that are capable of imaging thick tissue at high resolution with no tissue processing and that can automatically segment and quantify those specimens.

Part B – Rice University

Breast cancer is a leading cause of cancer mortality in women worldwide [52, 53], and although most patients are diagnosed with localized cancer, tumor size and presence of metastasis remain the main prognostic factors for survival [53, 54]. Current imaging tools provide limited ability to detect early lesions and to image relevant biomarkers *in situ*. Thus developing novel strategies for early detection of invasive and metastatic disease may have a significant impact on reducing patient morbidity and improving survival.

Traditional methods for early detection of breast cancer, including physical examination, mammography, ultrasound, and magnetic resonance imaging (MRI), are limited by low sensitivity and specificity for pre-malignant lesions [55-61]. In addition, these imaging methods do not give molecular information. As a result, histologic assessment is currently the reference standard for early diagnosis of breast cancer lesions and assessment of relevant biomarkers, which also typically requires immunohistochemical (IHC) staining. Both histologic assessment and IHC require biopsy, take extensive time to perform, and may need to be repeated in cases where lesions are missed due to sampling error. Histologic assessment has a limited ability to monitor response to targeted therapy, because of the need to obtain tissue specimens and the extensive time required to prepare and review tissue specimens.

Optical imaging approaches have the potential to address the limitations of traditional methods to detect breast cancer and monitor response to therapy and can provide the ability to image

lesions in real time with minimal invasion [27, 62-71]. With the introduction of fiber optic probes, images can be acquired intraoperatively or through needles with high spatial resolution to visualize subcellular morphology and tumor microenvironment [27, 63, 72]. It is also possible to add molecularly targeted, optically active contrast agents to image changes in biomarker expression [73]. A number of high resolution imaging approaches have been proposed to characterize breast lesions, including confocal reflectance and fluorescence microscopy, fiber optic microendoscopy (FOME).

The long term objective of this work is to develop and apply imaging systems and molecular contrast agents which can be used in patients to 1) improve early detection and rapid assessment of breast cancer lesions, 2) aid in selection of targeted therapeutics, and 3) monitor the efficacy of these therapeutics in real-time.

Feasibility of optical imaging techniques for imaging human breast tissue: 2011-2013

Breast cancer development is a complex process which occurs when atypical ductal hyperplasia progresses to low grade ductal carcinoma *in situ* (DCIS), a malignant precursor to invasive breast cancer [74]. Identification of DCIS is important for preventing the development of invasive breast cancer; however, it is difficult to distinguish DCIS – a malignant lesion - from ductal hyperplasia – a non-neoplastic lesion [75].

The current standard for breast lesion assessment is histologic assessment of tissue specimens stained with hematoxylin and eosin (H&E), which is limited by extensive preparation steps and time requirements. There is an unfulfilled need for clinical imaging tools to evaluate tumor margins, residual tumor in the resection bed, adequacy of core needle biopsy specimens for biobanking or genetic studies, and to monitor disease regression in response to treatments that are being tested in animal studies. Optical imaging techniques such as confocal fluorescence microscopy have the potential to meet these needs [69, 71, 73, 76-78]. Confocal fluorescence microscopy can be used in a clinical setting to acquire high resolution images of breast tissue architecture at near video rate. In addition, it can be performed on fresh tissue, and require minimal tissue preparation. The objective of this study was to determine whether images of fresh human breast tissue acquired with confocal fluorescence microscopy provide sufficient information to enable discernment of neoplastic and non-neoplastic breast features.

To meet this objective, the aims of this study were to:
   a. Characterize the microscopic architecture of normal, benign and neoplastic breast biopsies visible using confocal fluorescence microscopy
   b. Assess diagnostic accuracy of confocal fluorescence microscopy to assess breast architecture compared to the standard for breast lesion assessment: histology with H&E staining
   c. Quantitatively analyze metrics of morphologic changes associated with progression from non-proliferative and hyperplastic ducts to DCIS and to compare performance of these metrics for classification of DCIS in confocal and histologic images.

Methods:
We used a commercial confocal microscope (Vivascope 2500, Caliber Imaging and Diagnostics, Inc.) to image resected breast tissue and needle biopsy specimens (n = 129 specimens from 67 patients). There were 235 ROIs identified which had corresponding breast architecture in confocal fluorescence and histologic images. The images were assembled into a library to facilitate comparison between high resolution optical images and the corresponding histological sections (Figure 2.8).

Mean fluorescence intensity was assessed for its potential to identify neoplastic lesions from non-neoplastic lesions in confocal images. Images were normalized by the power used for image acquisition. A semi-automated algorithm was developed to measure mean fluorescence intensity at user-defined ROIs including normal, non-proliferative ducts, hyperplastic ducts, ductal carcinoma in situ, and invasive ductal carcinoma.

We developed a computerized algorithm to quantitatively analyze duct morphology in histologic and confocal images using parameters of ducts and lumens, including:

    i.   duct wall width (mean, standard deviation, and variance)
    ii.   number of lumens contained within the duct wall
    iii. major and minor dimensions of ducts and lumens
    iv. duct and lumen area
   v.   duct and lumen eccentricity
    vi. duct and lumen solidity

The best performing parameters for classifying DCIS from non-neoplastic ducts were identified using linear discriminant analysis and each parameter's performance was assessed using sensitivity, specificity, and area under the curve (AUC).

Results:
We organized a subset of images in the library into a training set (n = 23 ROIs) and a validation set (n =49 ROIs). These sets of images were visually assessed using standard criteria for histologic review by 7 readers: 5 experienced pathologists and 2 pathology fellows. Validation study results acquired following visual review of the validation sets (Figure 2.9) indicate that 1) neoplasia can be identified in confocal images with high sensitivity and specificity (Se = 93%, Sp = 93%), and 2) neoplasia can be identified in confocal images with similar accuracy compared to review of histologic images (Se = 93%, Sp = 97%).
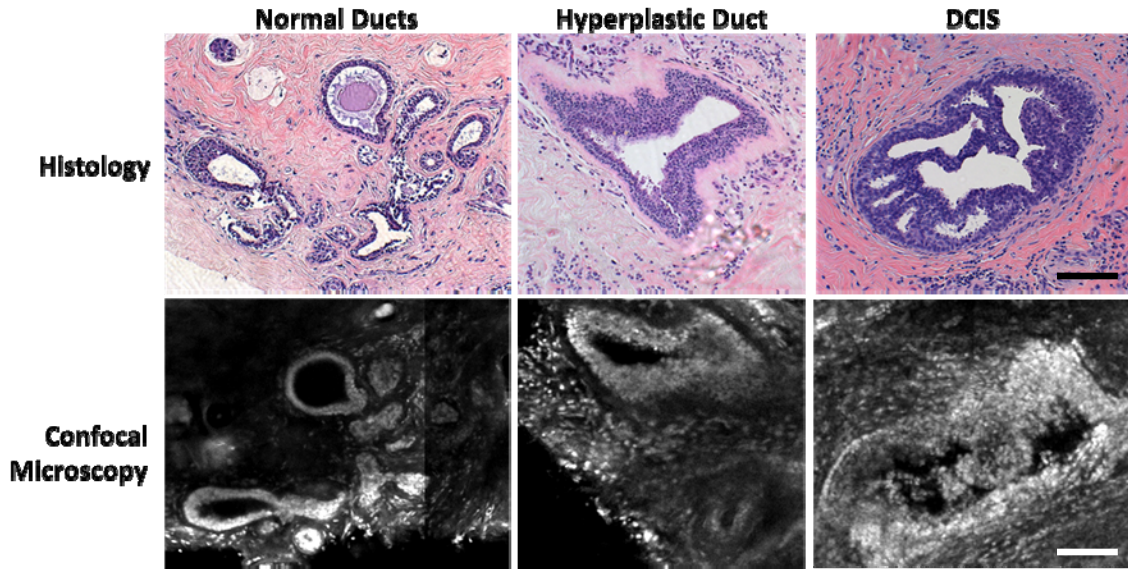
Figure 2.8: Architecture indicative of normal breast tissue (i.e. normal ducts), benign changes (i.e. hyperplastic ducts), and neoplastic disease (i.e. ductal carcinoma in situ, DCIS) were identified at corresponding sites in histologic and confocal images. Scale bar is 100µm.
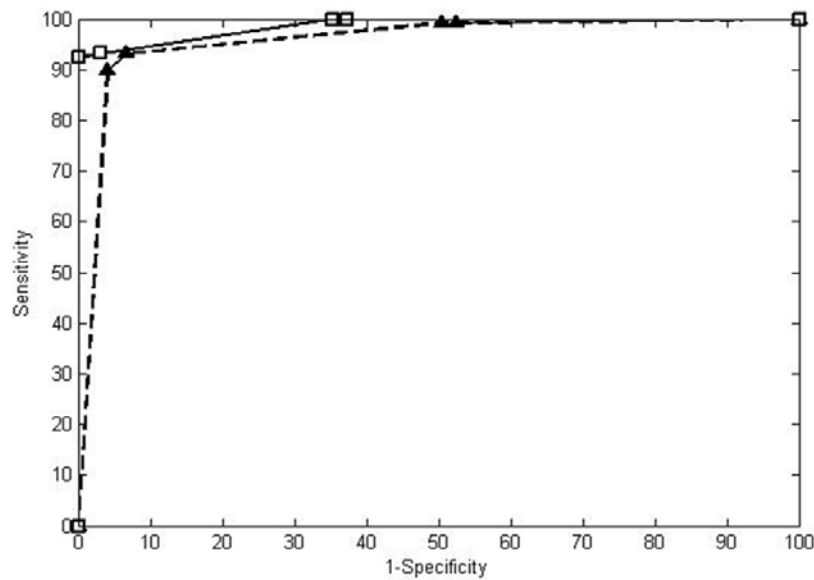
Figure 2.9: Receiver operator characteristic (ROC) curve for the averaged performance of all readers in distinguishing neoplastic from non- neoplastic breast architectural features in conventional histologic (square markers, solid line) and confocal fluorescence images (triangular markers, dashed line). At the Q-point of the ROC curve for histology performance, the sensitivity is 93% and the specificity is 97% with an area under the ROC curve of 0.987. At the Q-point of the ROC curve for confocal fluorescence microscopy performance, the sensitivity is 93% and the specificity is 93% with an area under the ROC curve of 0.957.

Mean fluorescence intensity was measured at sites in confocal fluorescence images illustrating non-neoplasia: normal, non-hyperplastic ducts (n=36) and ductal hyperplasia (n=17), and neoplasia: ductal carcinoma *in situ* (n=12) and invasive ductal carcinoma (n=25). The histologic diagnosis for all additional ROIs identified in confocal fluorescence images and assessed for

mean fluorescence intensity was verified by a dedicated breast pathologist. The mean fluorescence intensity of DCIS (intensely stained nuclei) is higher than IDC, normal ducts, and hyperplastic ducts, all described with weakly stained nuclei (Figure 2.10).
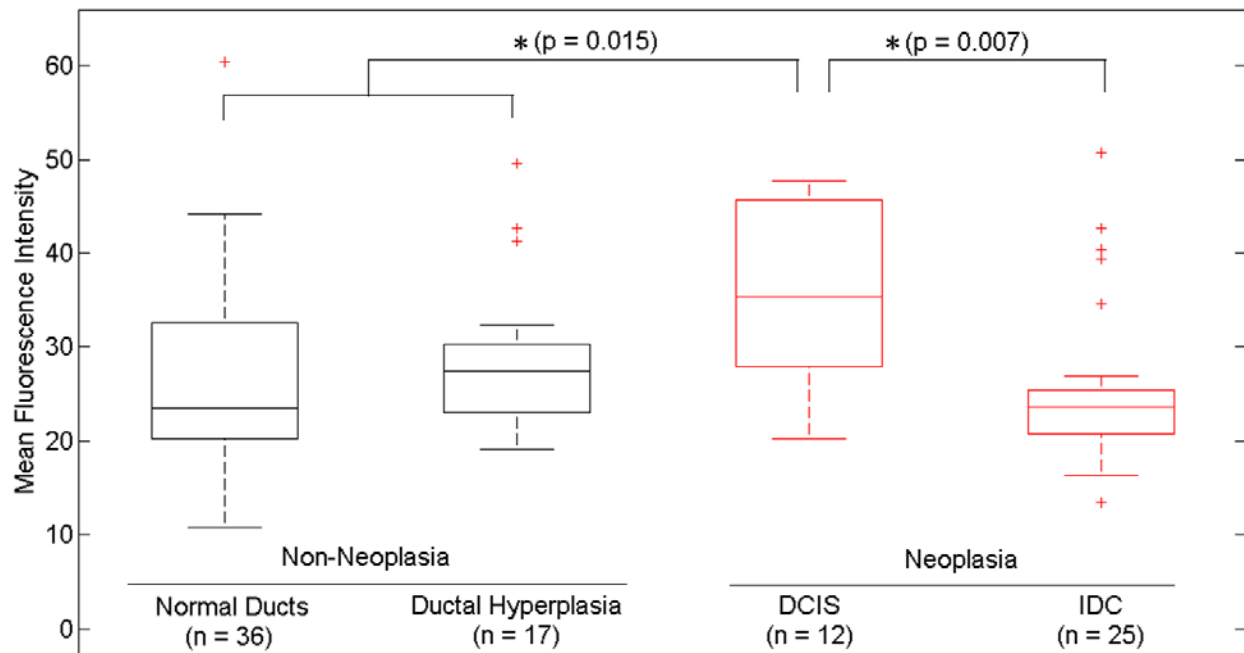

Figure 2.10: Differences in the mean fluorescence intensity of DCIS are statistically significant when compared to that of IDC (p = 0.007) and non-neoplastic ducts (p = 0.015). Mean fluorescence intensity values observed in normal ducts (26.6 ± 9.9), ductal hyperplasia (29.3 ± 8.2) and invasive ductal carcinoma (25.9 ± 8.8) were not significantly different (p > 0.05).

Parameters of ducts were quantified in histologic images (n = 181 sites) and in confocal images (n = 80 sites) acquired from 15 patients. The parameter which best classifies DCIS in confocal images is median duct wall width, which separates DCIS from non-neoplastic ducts with a sensitivity of 71% and a specificity of 86%, corresponding to an area under the curve of 0.88. The combination of two parameters which result in the best separation between DCIS and non-neoplastic ducts are median duct wall width and major duct dimension, which identify DCIS from non-neoplastic ducts with a sensitivity of 84% and a specificity of 84% (Figure 2.11).

The parameter which best identifies DCIS in histologic images is standard deviation of duct wall width, which separates DCIS from non-neoplastic ducts with a sensitivity of 78% and a specificity of 82%, corresponding to an area under the curve of 0.85. The combination of two parameters which result in the best separation between DCIS and non-neoplastic ducts are standard deviation in duct wall width and number of lumens contained within the duct wall, which identify DCIS from non-neoplastic ducts with a sensitivity of 78% and a specificity of 86% (Figure 2.12).

Parameters for quantitative analysis of duct morphology did not perform as well in identifying neoplastic lesions as subjective analysis by visual assessment; sensitivity, specificity, and AUC were lower for automated assessment in both confocal and histologic images.
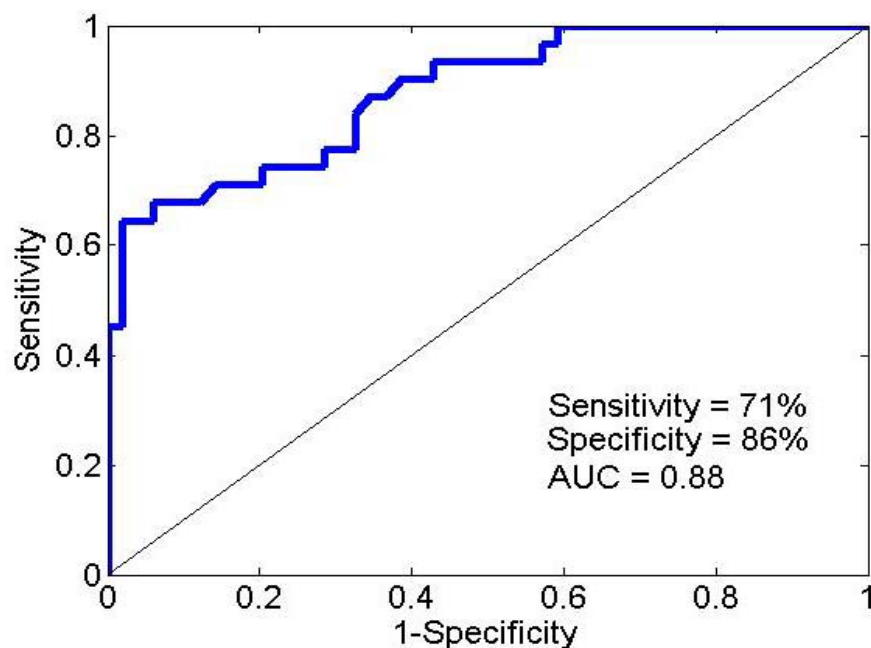
Figure 2.11: Classification of DCIS in confocal images. The parameter which results in the best separation between DCIS and non-neoplastic ducts identified in confocal images: median duct wall width (sensitivity = 71%, specificity = 86%, AUC = 0.88).
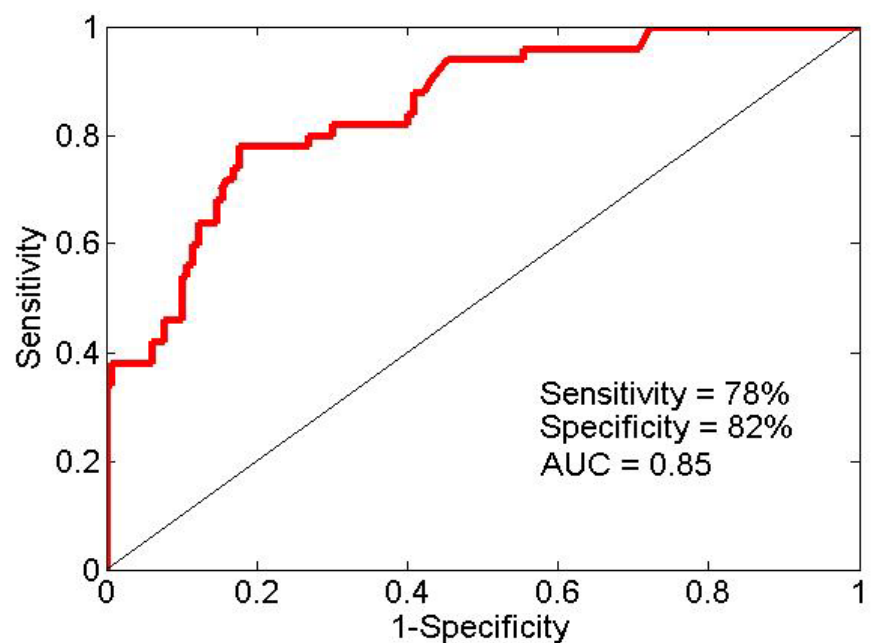
Figure 2.12: Classification of DCIS in histologic images. The parameter which results in the best separation between DCIS and non-neoplastic ducts identified in histologic images: standard deviation in duct wall width (sensitivity = 78%, specificity = 82%, AUC = 0.85).

Conclusions:

In this study, we evaluated breast architecture in confocal and histologic images based on visual criteria used for standard assessment of histologic images. We also evaluated mean fluorescence intensity as a possible parameter to characterize non-neoplastic and neoplastic breast architecture in confocal images. Using parameters of duct architecture, we quantitatively analyzed duct morphology in confocal and histologic images. Although objective analysis of duct morphology based on physical parameters of ducts showed a poorer performance for identification of neoplastic lesions than subjective assessment, we will continue to develop these parameters with the goal of developing methods to automate breast tissue assessment.

Findings of this study show that confocal fluorescence images of fresh human breast tissue provide sufficient information to enable discernment of neoplastic and non-neoplastic breast features based on visual assessment in a reader study and using mean fluorescence intensity and parameters of duct morphology for automated assessment. Parameters such as duct wall width, duct area, and number of lumens are associated with diagnostic categories of duct and that parameters had similar performance for classification of DCIS in both types of images. These data suggest that quantitative analysis of duct morphology in confocal fluorescence images could provide an objective way to assess duct histology and identify DCIS. This study has potential for use in clinical and research settings, including applications in 1) immediate evaluation of the adequacy of tissue core biopsy specimens procured with or without imaging guidance, 2) assessment of tumor margin status, which could be performed without the necessity for extensive tissue preparation while yielding results comparable to those of frozen section histology, and 3) ensuring procurement of adequate viable tumor tissue for molecular testing, and 4) evaluation of disease regression and progression in animal studies to assess novel treatment regimens. All reportable outcomes are based on this work.

**Adipocyte segmentation study: 2012-2013**

Extensive literature has shown that stromal components in the tumor microenvironment play a role in breast carcinoma progression and invasion [79-82]. It has recently been suggested that adipocytes located adjacent to tumors participate in crosstalk with invasive cancer cells through bi-directional paracrine signaling pathways, which affect processes such as tissue remodeling, adipogenesis and energy metabolism, oncogenesis, inflammation, and immune response [79]. The objective of this study is to use confocal fluorescence microscopy to evaluate morphological characteristics of adipocytes adjacent to neoplastic and non-neoplastic breast tissue to determine if there is a correlation between adipocyte morphology and clinical diagnosis.

Methods:

The confocal fluorescence images of tissue specimens acquired in the previous study were used as the basis for quantitative evaluation of adipocyte morphology adjacent to normal collagen and lesions on invasive ductal carcinoma. We developed an algorithm to automate segmentation of adipocyte cells, which was used to analyze adipocytes' cross-sectional area in confocal images (Figure 2.13).

Results:

Adipocyte area was measured in a total of 10 specimens: in 5 normal specimens and 5 neoplastic specimens.
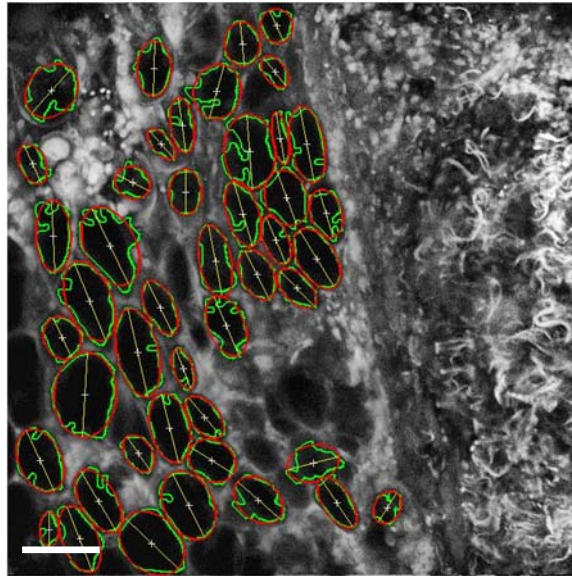
Figure 2.13: Automatic segmentation of adipocytes adjacent to a lesion of invasive ductal carcinoma using a computerized algorithm. Scale bar is 100μm.

Preliminary results show that the mean size of adipocytes adjacent to invasive ductal tumors is lower than the mean size of adipocytes adjacent to DCIS foci and in normal adipose tissue (Figure 2.14).
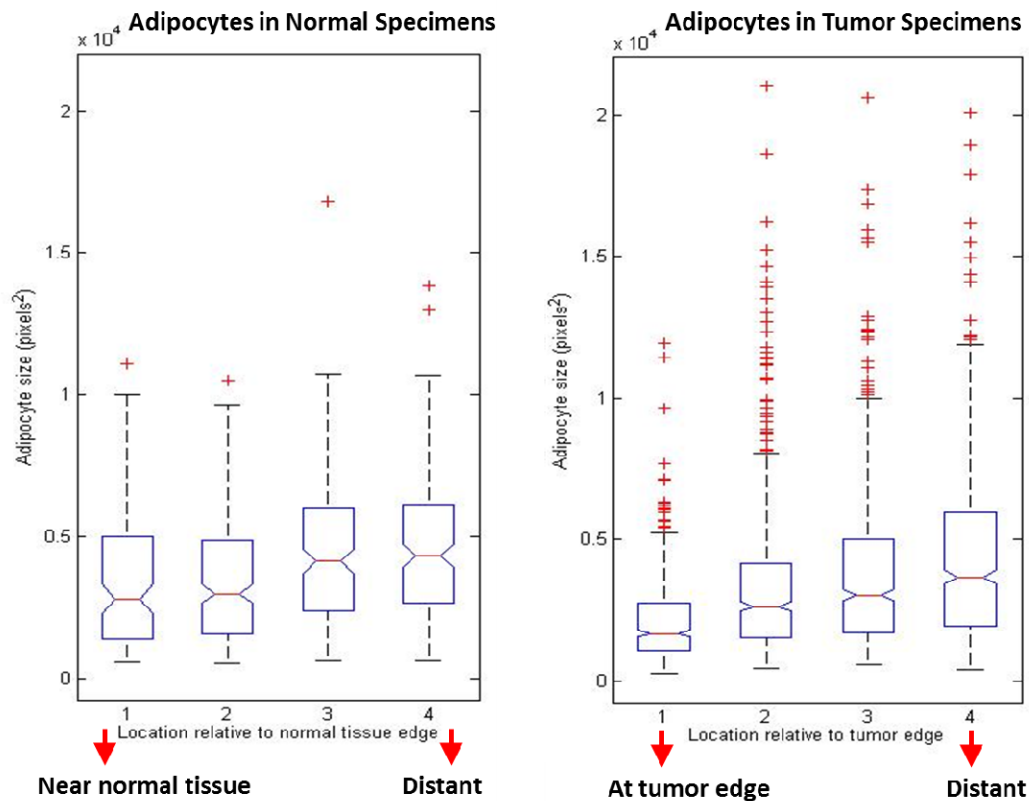
Figure 2.14: Preliminary results from automatic segmentation of adipocyte area measured adjacent to normal tissue and adjacent to tumors.

Conclusions:

The goal of this proposal was to develop and apply imaging systems and molecular contrast agents which can be used in patients to 1) improve early detection and rapid assessment of breast cancer lesions, 2) aid in selection of targeted therapeutics, and 3) monitor the efficacy of these.

Confocal fluorescence microscopy was compared to histology with H&E staining for classification of neoplastic lesions based on visual assessment and we found that readers identified neoplasia in confocal and histologic with similar accuracy. We demonstrated that mean fluorescence intensity, a parameter of confocal images, is significantly different in DCIS lesions vs. invasive carcinoma and non-neoplastic ducts. Thus, we show that confocal images of fresh human breast tissue provide sufficient information to enable discernment of neoplastic and non-neoplastic breast features, which has potential to improve rapid assessment of breast cancer lesions

Quantitative analysis of features of breast architecture, including adipocytes and ducts, shows that there are significant differences in breast morphology at neoplastic and non-neoplastic sites. We found that adipocyte area is lower when adjacent to some lesions of invasive ductal carcinoma than in normal tissue adjacent to collagenous tissue. Quantitative parameters of duct morphology such as duct wall width, duct area, and number of lumens are associated with

diagnostic categories of duct and that parameters had similar performance for classification of DCIS in both types of images. These findings indicate that physical parameters of breast morphology could be used to rapidly assess breast lesions and to monitor disease progression and regression.

Plans for next year:

Our goals for the coming year are to:

1. Explore the ability of optical biomarkers to discriminate DCIS from benign ductal changes. Our analysis will include ductal features as well as features of the surrounding microenvironment.
2. Explore the correlation between optical biomarkers of early breast cancer cells and their surrounding microenvironment with clinical parameters, including critical hormone status (i.e. estrogen receptor negative, HER2 positive, and triple negative receptor status), histologic degree of differentiation, lymph node status, and presence of distant metastases.

Our long term goal is to develop tools to facilitate early diagnosis of breast cancer by improving the ability to identify in real time whether breast biopsies have adequately sampled the lesion under investigation and to facilitate effective surgical treatment by improving the ability to adequately survey the tumor bed for residual DCIS disease.

Aim 3: *Optical imaging of tumor metabolism to predict long-term fate*

The currents goals of Aim 3 include the study of tumor metabolic and vascular response to stress in cell lines that were bound by a common theme – metastatic or non-metastatic, radiosensitive or radioresistant. In Year 4, we have made good progress towards achieving the goals stated in our previous report's Year 4 plans. First, we published the results detailed in the previous report reporting the combined measurement of oxygenation and glucose uptake in dorsal skin flap window chambers (*Rajaram PLoS ONE 2013*). We found that uptake of a fluorescent glucose marker, 2-NBDG, was influenced by the rate at which it was delivered to tissue. We also found that the delivery-corrected glycolytic demand of the metastatic 4T1 tumors was significantly higher than the non-metastatic 4T07 tumors. Second, we used a combination of glucose uptake and vascular oxygenation to study the radiation response of 4T1 tumors (*Zhong Radiation and Oncology 2013*). We found a large increase in vascular oxygenation and a corresponding increase in 2-NBDG uptake indicating a potentially aerobic glycolysis phenotype. Aerobic glycolysis has been implicated as a cause for resistance to radiation. Our future work entails determination of long-term outcome in animals that show an aerobic glycolysis phenotype.

Third, to further study the effects of delivery of 2-NBDG uptake and how the delivery rate could be used to correct glycolytic demand, we carried out a series of experiments in normal tissue where we varied the dose of 2-NBDG injected and used a stereoisomer of 2-NBDG to measure

the delivery and uptake of a non-specific marker – 2-NBDLG. Based on these experiments, we derived a delivery-corrected ratio glycolytic demand term that more accurately represents *in vivo* glycolytic demand. These data are currently in preparation for manuscript submission.

Finally, we determined the feasibility of clinically translational optical spectroscopy to noninvasively quantify *in vivo* glucose uptake in tissue and solid tumors. We found that optical spectroscopy was exquisitely sensitive to 2-NBDG absorption and not just fluorescence. 2-NBDG absorption was significantly different in tumors compared to normal tissue and increased proportional to fasting duration. These results are currently in preparation for manuscript submission.

Our progress in Aim 3 is divided into sections – High-resolution imaging and optical spectroscopy.

Part A: High resolution imaging of tumor microenvironment

Introduction:

The future of cancer management lies in the development of effective tumor-specific therapy. Every year, thousands of benign cancers such as ductal carcinoma in situ (DCIS) are managed the same way as more malignant forms of breast cancer. Efforts in the cancer community have been devoted to developing 'personalized medicine' by characterizing the genomic profiles of tumors. However, it is becoming evident that a single tumor can exhibit large spatial heterogeneities in genotype, making genomic profiling-based treatment a tough task [83]. Tumors of the same organ also differ in the hallmarks they exhibit, such as loss of function of tumor suppressors or gain of function of oncogenes. In spite of these variations in molecular events and signaling pathways, almost all cancers exhibit a common *phenotype* – increased glucose metabolism relative to normal cells [84]. Although the switch to glycolysis is mediated by hypoxia and hence, hypoxia-inducible factor (HIF) activity,[85] several tumors retain the same phenotype even in the presence of oxygen – a phenomenon first observed by Otto Warburg and hence named the Warburg effect or aerobic glycolysis [86].

Developing a strategy to image the tumor microenvironment is important for two reasons. First, the microenvironment provides clues about the cancer cells and their current state (diagnosis). Second, it provides a window into what might happen next because the tumor microenvironment itself causes changes to cell behavior (long-term behavior).

Our long-term goal is to determine whether the oxygenation-metabolic demand relationship changes in a tumor in response to stress and whether this response or change can be indicative of long-term tumor behavior. In this report, we describe the steps we have taken to progress towards our goal and lay out our plan for the next year.

Methods:

In vitro cell culture

4T1 and 4T07 murine mammary adenocarcinoma lines were cultured in Dulbecco's Modified

Eagle Medium (DMEM) supplemented with 10% fetal bovine serum (FBS) and 1% antibiotics. For imaging experiments, the cells were trypsinized and seeded on 60mm tissue culture plates 24 hours before imaging according to established protocols.

Dorsal skin flap window chamber model

All *in vivo* experiments were conducted according to a protocol approved by Duke University Institutional Animal Care and Use Committee. We surgically implanted titanium window chambers on the back of female athymic nude mice (nu/nu, NCI, Frederic, Maryland) under anesthesia (i.p. administration of ketamine (100 mg/kg) and xylazine (10 mg/kg)). We injected a 20 μL suspension (20,000 cells) of 4T1-RFP or 4T07 cells into the dorsal skin fold and placed a glass coverslip (dia = 12 mm, No. 2, Erie Scientific, Portsmouth, New Hampshire) over the exposed tissue. In a separate group of control mice, we injected 20 μL of saline. All animals were housed in an on-site housing facility with *ad libitum* access to food and water and standard 12-hour light/dark cycles. A flowchart depicting the experiment protocol is presented in **Figure 3.1.** For baseline measurements, the animals were kept in a chamber filled with 21% oxygen for 6 hours. For cycling hypoxia, the animals were exposed to alternating 1-hour cycles of 21% oxygen and 10% oxygen for 6 hours. During this 6-hour period, the animals were only provided with water. For *in vivo* studies alone, 4T1 cells were transduced by retroviral siRNA to constitutively express the red fluorescent protein (RFP) DsRed, allowing easy demarcation and growth tracking of tumor cells *in vivo*.

Radiation studies

Mice were injected with 4T1 tumor cells that were stably transfected with red fluorescence protein under control of a constitutive promoter (RFP), allowing tumors to be visualized using intravital fluorescence microscopy in skinfold window chambers. Mice were randomized to receive SOD mimic treatment +/- radiation, or no treatment. The study design is shown in **Fig. 3.1**. Tumor areas were measured by identifying pixels that were positive for RFP. There was not a significant difference in tumor area between the treatment groups ($p > 0.05$). After IV injection of 2-NBDG, the average fluorescence of 2-NBDG for tumor (defined as RFP (+) pixels) was recorded for 75 minutes. Signal Enhancement Ratio (SER) values for each tumor was also calculated for all mice. The distributions of SER values on a pixel by pixel basis for each animal were used to generate cumulative frequency histograms. These values were compiled for each group. This method of analysis facilitates comparisons between treatment groups and has been used previously by Hardee et al [87].
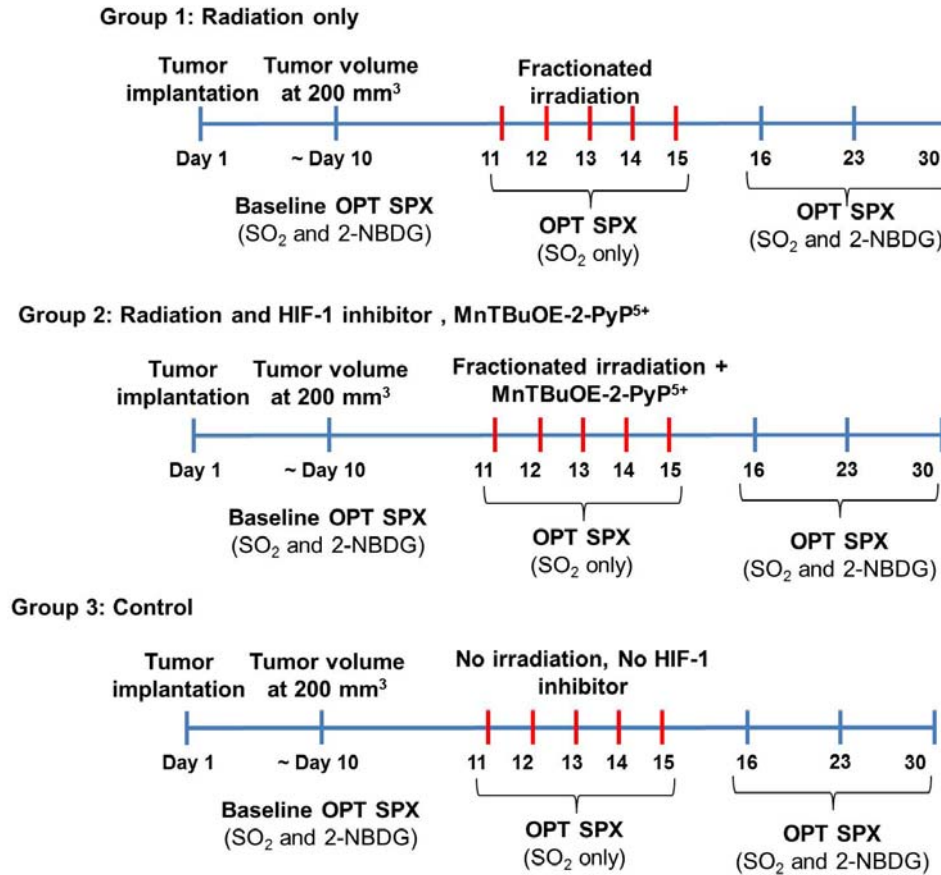
Figure 3.1. Study design of the radiation studies. Not shown here is a separate group that received only the HIF-1 inhibitor.

## Hyperspectral imaging of oxygen saturation and glucose uptake

A schematic of our study design is shown in **Fig. 3.1**. We used a Zeiss Axioskop 2 microscope for recording all images. At the end of 6 hours of fasting, we initially recorded trans-illumination images, RFP fluorescence (for 4T1-RFP cells) and corresponding background images. In addition, a free space trans-illumination image using appropriate neutral density filters was recorded before every imaging session to account for daily variations in light intensity. The animals were administered a 100 μL tail-vein injection of 2-NBDG (6mM; MW: 342.16) dissolved in sterile saline. We recorded the 2-NBDG fluorescence 75 minutes as follows: Continuously for the first 8 minutes, every 30 seconds for the next 30 minutes and every 3 minutes for the final 35 minutes of imaging. A modified form of the Beer-Lambert law that describes absorption of chromophores in thin slices is fit to the trans-illumination image cube (x,y,λ) to obtain the concentration of the primary absorbers – oxy $[O_2Hb]$ and deoxy-hemoglobin $[dHb]$ at each pixel [88]. This is possible due to knowledge of the extinction coefficients of both absorbers. Based on this information, we can calculate total hemoglobin content $[THb = O_2Hb + dHb]$ and oxygen saturation of hemoglobin $[HbSat = O_2Hb/THb]$ at each pixel. Because THb is negligible in tissue space (hemoglobin exists in blood vessels only), we used THb to segment the blood vessels and create a map of vascular HbSat.
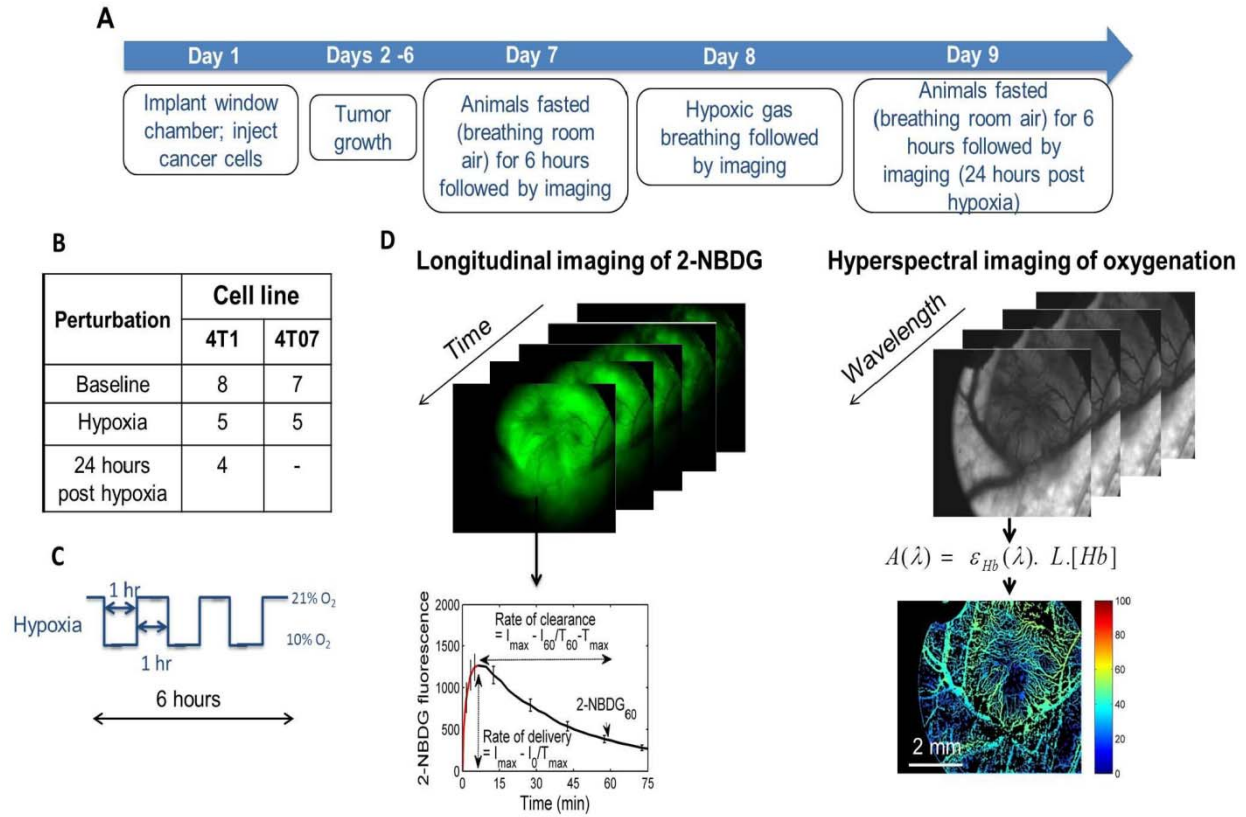
Figure 3.2: Methods. A. Flowchart describing study design. **B.** Sample size for the study. **C.** Illustration of hypoxia protocol. **D.** 2-NBDG fluorescence images are acquired continuously for a period of 75 minutes to construct a (x,y,λ) data cube. B) At each (x,y) pixel location, a time course of 2-NBDG uptake can be obtained. Based on the time course, three metabolic parameters can be calculated: the initial rate of delivery (R_D), rate of clearance (R_C), and glucose uptake (2-NBDG_{60}). C) Trans-illumination image cube of hemoglobin absorption is obtained from 520-620 nm. Total hemoglobin content is calculated pixel-wise by fitting a Beer-Lambert equation to the hyperspectral dataset. Knowledge of the wavelength-dependent extinction coefficients of hemoglobin allows calculation of oxy-hemoglobin and deoxy-hemoglobin concentrations. The ratio of oxy-hemoglobin to total hemoglobin concentration is the vascular oxygenation (SO_2).

Results:

### Radiation induced metabolic changes coincide with reoxygenation, suggesting aerobic glycolysis [89]
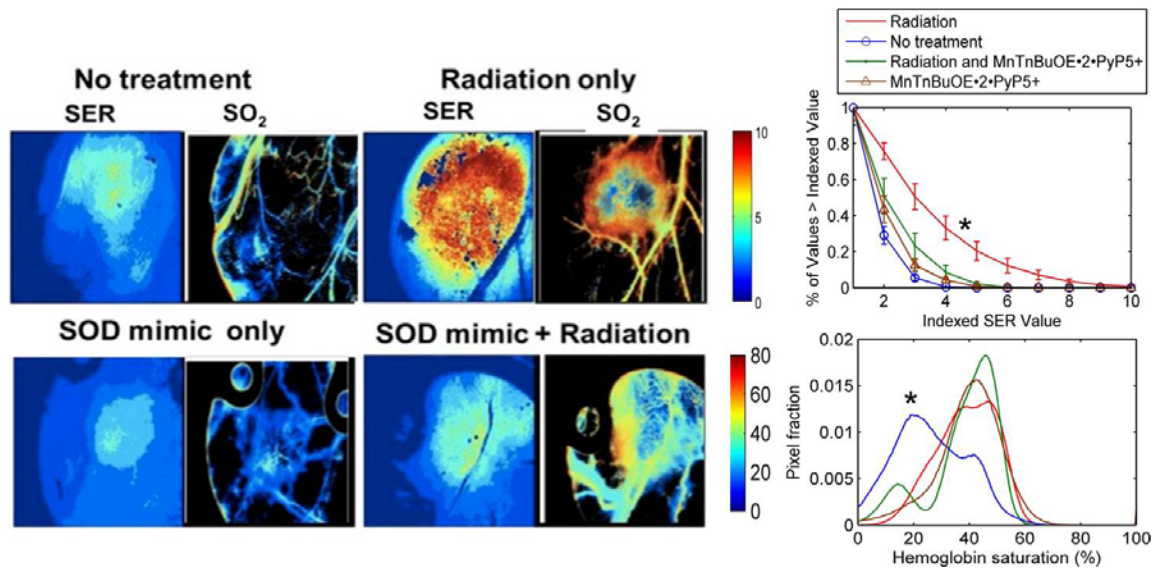
Figure 3.3. Radiation increases glucose uptake and oxygenation in irradiated 4T1 tumors. A. Representative SER image for all treatment groups: a) No treatment, b) Radiation alone, c) SOD mimic and Radiation, d) SOD mimic alone. **B.** Cumulative distribution functions of SER values for all treatment groups indicate that SER values for radiation only group are significantly higher ($p < 0.007$) than the other groups, which are not statistically different. Error bars depict standard error of the mean. **C.** Histogram displaying tumor vascular hemoglobin saturation in each treatment group. The y-axis represents the frequency of the pixels determined to be vasculature that displayed the corresponding hemoglobin saturation on the x-axis. The no treatment control group appeared to have a significantly lower hemoglobin saturation compared to the other three groups ($p = 0.009$), which were not statistically different from each other.

It is has been previously shown that HIF-1 activity and consequent anaerobic metabolism increased approximately 12-24 hours after radiation in the 4T1-RFP tumor line. The increase in HIF-1 activity was associated with reoxygenation induced reactive oxygen species [90, 91]. Since HIF-1 is known to regulate most enzymes involved in glycolysis, we sought to determine whether a reduction in reactive species via the use of the SOD mimic, MnTnBuOE-2-PyP5$^+$, can reduce glucose demand. Tumors in the irradiated group had higher peak 2-NBDG fluorescence compared with the no treatment control, at 3 and 6 minutes ($p < 0.05$). SER values obtained from the irradiated group were significantly higher ($p = 0.007$) than the other experimental groups, which were indistinguishable from each other (**Fig. 3.3**). Given that radiation appears to alter tumor glucose demand, we sought to determine whether these changes could be correlated temporally with reoxygenation. Hyperspectral images captured from the tumors were used to simultaneously calculate hemoglobin saturation of the tumor vasculature and 2-NBDG fluorescence. The tumors in the irradiated treatment groups displayed significantly higher hemoglobin saturation than the no treatment controls ($p = 0.009$). These findings strongly suggest that the radiation treatments increased tumor oxygenation. The SOD mimic only group appeared to display improved oxygenation as well, consistent with previous findings elucidating its anti-HIF/VEGF effects [92]. Altogether, these results are consistent with previous views regarding post-radiation tumor reoxygenation [90, 93, 94]. The finding that irradiated tumors increase glucose consumption in the presence of reoxygenation strongly suggests initiation of glycolysis rather than oxidative phosphorylation. Additionally while the treatment group receiving radiation concurrently with the SOD mimic demonstrates elevated hemoglobin saturation consistent with reoxygenation, the tumors demonstrate lower glucose demand. Consequently,

this data additionally suggests that post-radiation aerobic glycolysis was prevented by scavenging of oxidative reactive species and downstream HIF-1 upregulation, without compromising the reoxygenation process.

2-NBDG delivery (R_D) and uptake (2-NBDG$_{60}$) *in vivo* are influenced by changes in blood flow [95]
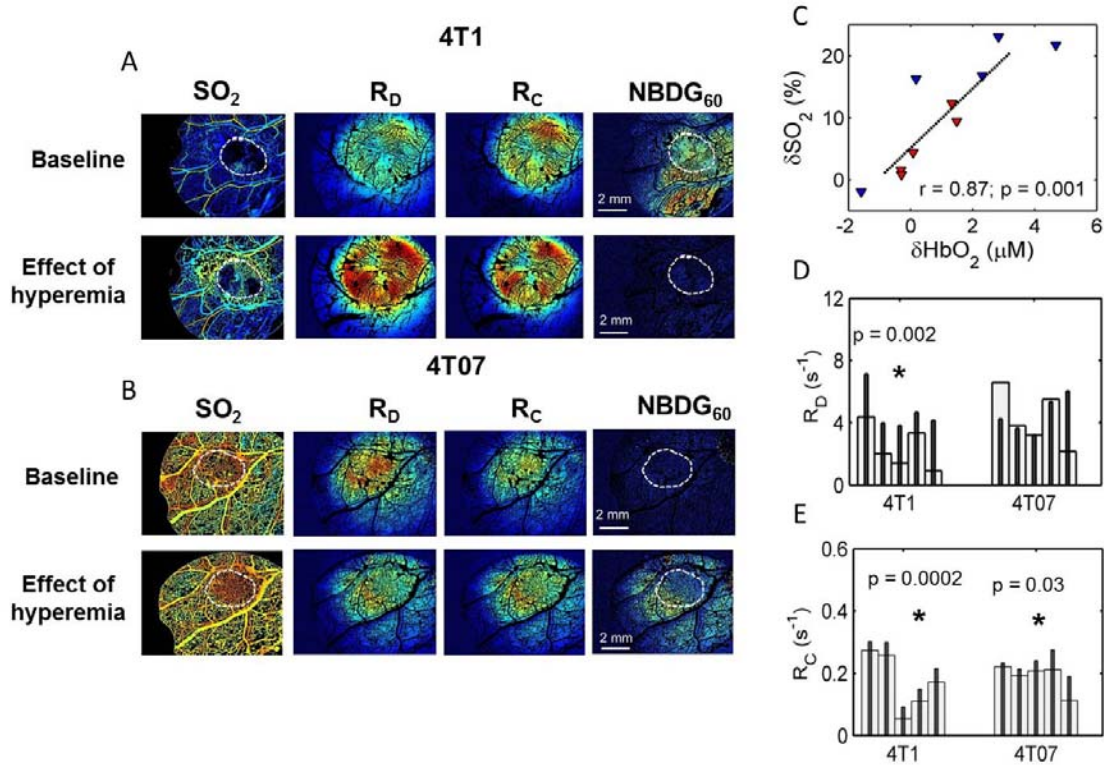
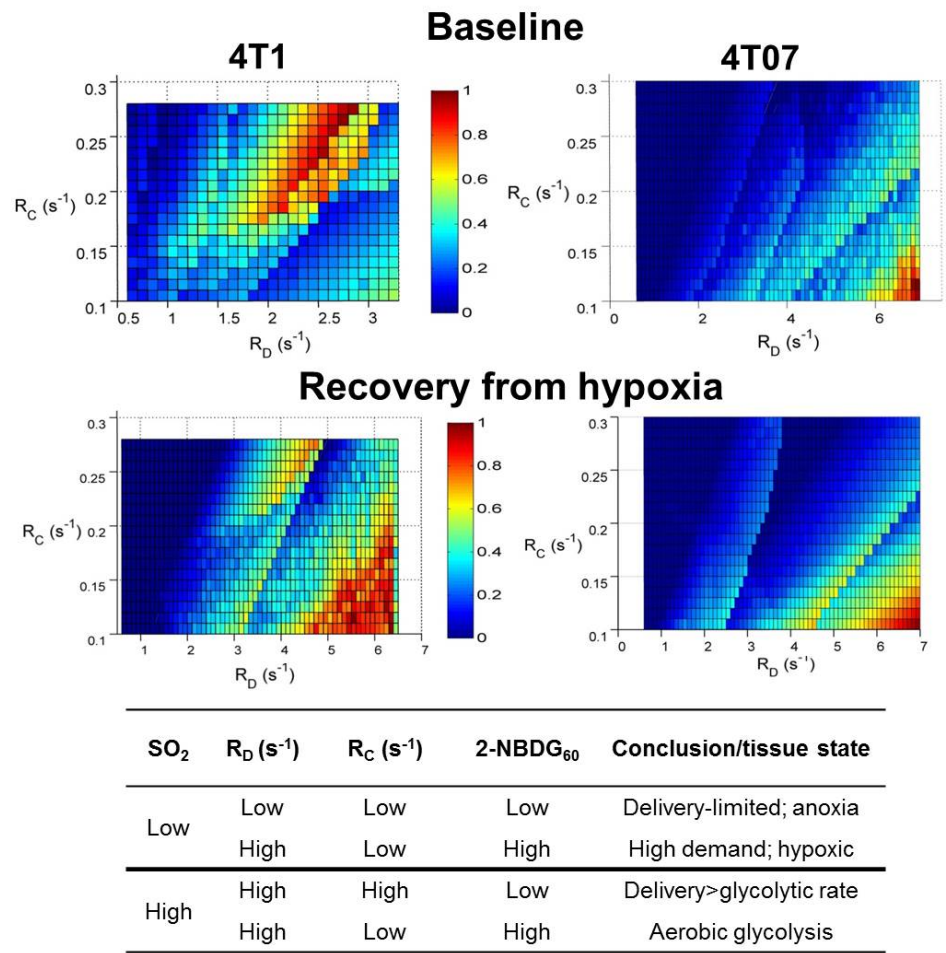
Figure 3.4: Effect of breathing hypoxic gas on vascular oxygenation and glucose uptake of 4T1 and 4T07 tumors. A and B. Representative intravital images of vascular oxygenation (SO$_2$) and glucose uptake from 4T1 and 4T07 tumors at baseline and after breathing hypoxic gas (10% O$_2$, rest N$_2$). White dotted line in each image represents the tumor. **C.** The change in SO$_2$ of 4T1 and 4T07 tumors after hypoxia is strongly correlated with a change in oxy-hemoglobin concentration (r = 0.87; p = 0.001). **D.** Breathing hypoxic gas caused a significant increase in R_D of 4T1 tumors (p = 0.002). **E.** There was significant increase in R_C of 4T1 and 4T07 tumors after breathing hypoxic gas. Each set of bars in D and E represents data from one animal at baseline and after hypoxia (5 animals per cell line).

Figure 3.4 shows representative images of SO$_2$ and 2-NBDG$_{60}$ from the 4T1 and 4T07 tumors at baseline and after breathing hypoxic gas (hyperemia). Breathing hypoxic gas significantly increased SO$_2$ of the 4T1 tumors (p = 0.03). Although SO$_2$ in 4T07 tumors increased after hypoxia, this was not statistically significant (p = 0.06). The increase in SO$_2$ was strongly, but negatively associated with baseline SO$_2$ in both cell lines (r = 0.74, p = 0.01). Further, the increase in SO$_2$ was driven by an increase in [HbO$_2$] (r = 0.87, p = 0.001), reflecting increased blood flow in both cell lines after breathing hypoxic gas. The increased blood flow caused a significant increase in R_D of 4T1 tumors (p = 0.002) and R_C of the 4T1 (p = 2x10^{-4}) and 4T07 tumors (p = 0.03). At baseline, mean 2-NBDG$_{60}$ of the 4T1 tumors is significantly higher than the

4T07 tumors ($p<0.05$). After breathing hypoxic gas, mean 2-NBDG$_{60}$ decreases in the 4T1 tumors and increases in the 4T07 tumors. Because 2-NBDG$_{60}$ was not directly correlated with SO$_2$, these data imply that the R$_D$ of 2-NBDG influences uptake in both the 4T1 and 4T07 tumors. However, there does not appear to be a simple relationship between the two parameters. Therefore, the relationship between R$_D$, R$_C$ and 2-NBDG$_{60}$ for the 4T1 and 4T07 tumors was analyzed next.

R$_D$ in excess of glucose consumption rate leads to lower 2-NBDG$_{60}$

SO$_2$	R$_D$ (s^{-1})	R$_C$ (s^{-1})	2-NBDG$_{60}$	Conclusion/tissue state
Low	Low	Low	Low	Delivery-limited; anoxia
	High	Low	High	High demand; hypoxic
High	High	High	Low	Delivery>glycolytic rate
	High	Low	High	Aerobic glycolysis

Figure 3.5: Relationship between SO$_2$, R$_D$, R$_C$ and 2-NBDG$_{60}$ for 4T1 and 4T07 tumors. A. Contour plots showing the relationship between delivery, clearance and uptake of 2-NBDG. R$_D$ and R$_C$ represent the x- and y-axes, respectively, while 2-NBDG$_{60}$ represents the z-axis projecting out of the x-y plane. For the 4T1 tumors at baseline, 2-NBDG$_{60}$ increases with R$_D$ at low values of R$_C$. At higher values of R$_C$, 2-NBDG$_{60}$ reaches a maximum at R$_D$ = 2.5 s^{-1}, levels off and then declines gradually for increasing R$_D$. After hypoxia, a secondary maximum is seen at very high values of R$_D$ (R$_D$ > 6 s^{-1}) and low R$_C$. In the 4T07 tumors, 2-NBDG$_{60}$ increases with R$_D$ and reaches a maximum at approximately 6 s^{-1}. The same feature is also present after hypoxia. At higher values of R$_C$, 2-NBDG$_{60}$ was nearly negligible for increasing values of R$_C$. **B.** A summary of possible relationships between NBDG$_{60}$, R$_D$, R$_C$, and SO$_2$ and final outcome corresponding to each combination.

Figure 3.5 presents the relationship between R$_D$, R$_C$ and 2-NBDG$_{60}$. R$_D$ and R$_C$ represent the x- and y-axes, respectively, while 2-NBDG$_{60}$ represents the z-axis projecting out of the x-y plane.

The data shown here are from all tumors within a group. For the 4T1 tumors at baseline, the R_D range is 0.5 - 3 s^{-1}. 2-NBDG$_{60}$ is lowest when R_D and R_C are low (lower left quadrant) and corresponds to poorly oxygenated tumor regions, indicating perfusion-limited uptake. When R_D increases, there is a corresponding increase in 2-NBDG$_{60}$ and R_C, indicating higher uptake due to improved delivery. When R_D exceeds approximately 2.5-3 s^{-1}, 2-NBDG$_{60}$ plateaus and declines with any further increase in R_D. This effect is observed clearly at high values of R_C (>0.2 s^{-1}). The inflection point in the 4T1 tumors at baseline of 2.5-3 s^{-1} is approximately equal to the glucose consumption rates calculated *in vitro*, demonstrating that R_D in excess of the glucose consumption rate leads to a decrease in 2-NBDG$_{60}$. After hypoxia, the R_D range extends to 6s^{-1}. The 4T1 tumors exhibit a similar decline in 2-NBDG$_{60}$ beyond the glucose consumption rate; however, there is a slight shift in this inflection point to ~4s^{-1}, suggesting an increase in the glucose consumption rate after breathing hypoxic gas. Due to higher rates of delivery in the 4T07 tumors, regions with R_D values < 3.5 s^{-1} are mostly absent and the inflection point is not observed. Similar to the 4T1 tumors after hypoxia, a 2-NBDG$_{60}$ maximum exists at high R_D (> 6 s^{-1}) and low R_C (< 0.15 s^{-1}). This is also observed in the 4T07 tumors after hypoxia.

The table in **Fig. 3.5** summarizes the interplay seen in the contour plots between the three metabolic endpoints and their relationship to SO_2. Regions of low 2-NBDG$_{60}$ do not necessarily mean anoxic tissue and delivery limitations; they can also indicate regions of high SO_2 with delivery rate exceeding the glycolytic rate. Similarly, a high level of 2-NBDG$_{60}$ may not mean hypoxic tissue with great demand; it could potentially indicate tumors demonstrating aerobic glycolysis.

<u>Delivery-corrected 2-NBDG uptake provides a better representation of glycolytic demand</u>
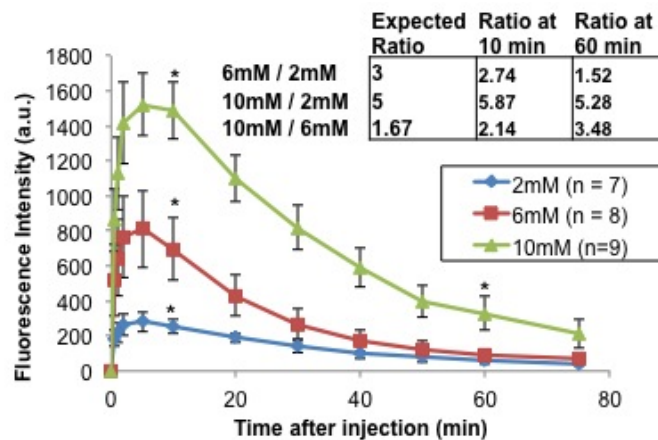
Figure 3.6. Variation in injected dose affects 2-NBDG uptake in normal murine tissue. At early timepoints, 2-NBDG fluorescence scales linearly with injected dose (2mM<6mM, p=0.05 ;6mM<10mM p=0.01). At late timepoints, 10mM fluorescence is still greater than 2mM or 6mM (p=0.05), though the intensity dose not scale proportionally with dose.

Figure 3.6 shows group averages of fluorescence intensity for three different concentrations of 2-NBDG measured in normal murine window chambers. 2-NBDG was injected at concentrations of 2, 6, or 10mM and imaged for 75 minutes. Average values by concentration show that, in normal tissue, fluorescence intensity scales linearly with dose at early timepoints after injection

(2mM<6mM, p=0.05 ;6mM<10mM p=0.01), indicating that early fluorescence is dominated by injected dose. By 60 minutes, fluorescence intensity is no longer proportional to dose, but some delivery effect persists and must be taken into account (10mM > 2 or 6mM, p=0.05). The study in normal tissue confirms our previous studies in tumors that indicated that delivery effects are an important consideration when calculating the glucose demand of tissue i*n vivo.*
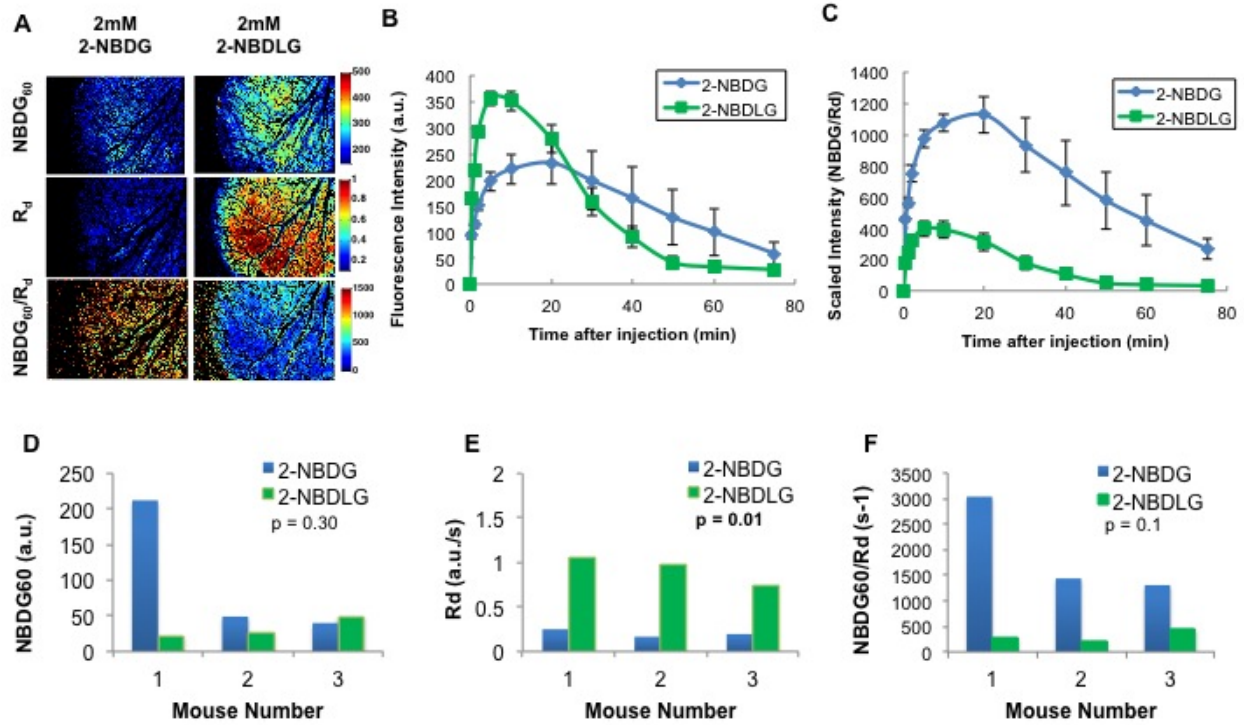
Figure 3.7. Dose-corrected 2-NBDG uptake accurately reports on demand in normal murine tissue. A. Representative images show $NBDG_{60}$, R_d, and $NBDG_{60}/R_d$ for normal tissue injected with 2-NBDG or the control 2-NBDLG. **B.** An uncorrected curve shows group averages of fluorescence intensity over time are similar for 2-NBDG or control 2-NBDLG. **C**. Fluorescence intensity corrected by delivery clearly shows increased demand for 2-NBDG relative to 2-NBDLG. **D.-F.** $NBDG_{60}$, R_d, and $NBDG_{60}/R_d$ separated by mouse show gives a clear view of high 2-NBDG demand relative to 2-NBDLG demand in each mouse. n=3 mice per group.

Figure 3.7 demonstrates our use of the 2-NBDG control, 2-NBDLG, in normal murine window chambers. 2-NBDLG has the same fluorescence properties as 2-NBDG, but it is not recognized or transported into the cell by GLUT receptors. As seen in the top row of images in **Figure 3.7A**, if not corrected for delivery, 2-NBDG and 2-NBDLG uptakes look comparable 60 minutes after injection, indicating that demand is similar for both fluorophores. However, when uptake at is corrected for delivery (R_d), 2-NBDG demand far exceeds 2-NBDLG demand in each mouse (**Figure 3.7A**). Averaged curves show un-corrected fluorescence intensity (**Figure 3.7B**) and fluorescence intensity corrected by rate of delivery (**Figure 3.7C**) for 2-NBDG and 2-NBDLG. Error bars show standard error. By 60 minutes, the corrected graphs accurately report on demand, which should be close to zero for 2-NBDLG after wash-out of the extracellular probe, and demand-dependent for 2-NBDG. The bottom row of charts (**Figure 3.7D-F**)shows $NBDG_{60}$, R_d, and $NBDG_{60}/R_d$ separated by each mouse treated with either 2mM 2-NBDG or 2mM 2-

NBDLG. Correcting for high delivery and flurorescence of 2-NBDLG magnifies the difference between high demand (2-NBDG) and no demand (2-NBDLG).
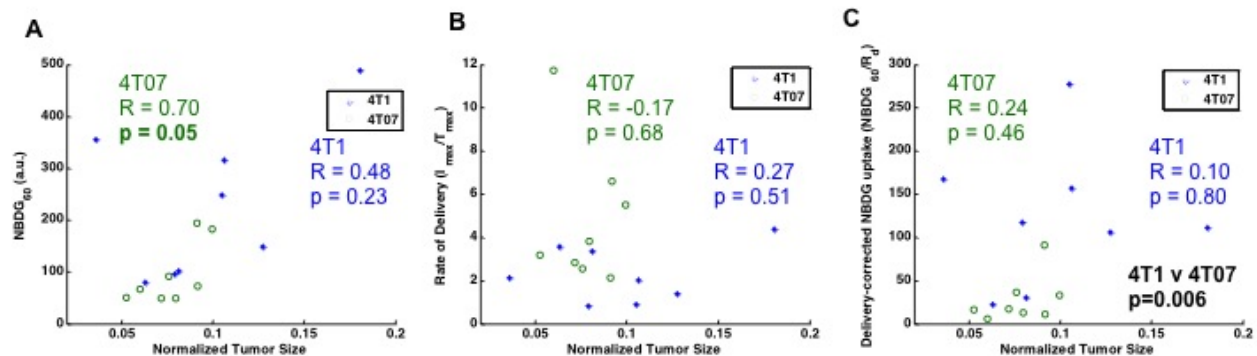
Figure 3.8. Dose-corrected 2-NBDG uptake distinguishes tumor types across a range of tumor sizes. A. $NBDG_{60}$ as a function of tumor size for 4T1 and 4T07 murine mammary tumors. 2-NBDG uptake increases significantly with tumor size for 4T07 tumors. **B.** Rate of delivery does not correlate with tumor size in either tumor line. **C.** Correcting for delivery leaves no dependence on tumor size, but distinguishes 4T1 from 4T07 (p=0.006). Tumor size was calculated as the ratio of tumor-positive pixels divided by total murine tissue pixels in a given murine window chamber image. n = 8 mice/tumor type.

Figure 3.8 shows a comparison of 4T07 and 4T1 murine mammary tumors, as a function of tumor size (tumor pixels/total tissue pixels). Only the 4T07 tumor line shows dependence of 2-NBDG uptake on tumor size, as 4T1 tumors tend toward high glucose uptake regardless of tumor size. Interestingly, rate of delivery does not show a significant dependence of tumor size in either line. After correcting for delivery, the two tumor lines are clearly distinguished, with the highly metastatic 4T1 line showing consistently higher corrected uptake than the 4T07 tumors, which display behavior similar to normal tissue. Though there seems to be no dependence of corrected uptake on tumor size, this is consistent with our expectation that R_d may be able to correct for changes in perfusion that occur with angiogenesis during tumor growth. It should be noted that $NBDG_{60}$ alone can distinguish the two tumor types in this study (p=0.03), but correcting for delivery decreases the intra-group variation and makes the separation between groups much more apparent (p=0.006).

Part B: Optical spectroscopy for clinical translation

Introduction
The classical approach to measurement of aerobic glycolysis involves glucose uptake and lactate production in the presence and absence of oxygen; cells inclined towards aerobic glycolysis show little to no change in glycolytic endpoints under hypoxic conditions. Studies *in vivo* have typically involved correlating specific oncogenic mutations that promote aerobic glycolysis with aggressive tumor growth (by measuring tumor volume) or staining excised tumor slices for markers of hypoxia after imaging with FDG-PET. Given the dynamic nature of changes in a tumor and especially in response to therapy, it is important to be able to repeatedly measure tumor bioenergetics *in vivo* and not just oxygenation or tumor glucose demand. Such a technique can be beneficial for studying tumor response to therapy and understanding changes in the tumor micro-environment in pre-clinical animal models. Here, we describe our efforts to develop a spectroscopic approach to measuring tumor bioenergetics *in vivo*. Our goal is to

translate findings from high resolution imaging of the tumor microenvironment to rapid, point of care technology.

Methods

Tissue-simulating phantoms

Tissue simulating phantoms that had varying amounts of absorption, scattering and fluorophore concentrations were prepared. Hemoglobin (H0267, Sigma-Aldrich Co., St. Louis, MO) was used as the non-fluorescent absorber and 1 µm monodisperse polystyrene spheres (1-µm diameter, Catalog No. 07310, Polysciences, Warrington, PA) were used as the scatterer in tissue mimicking phantoms. Mixing known volumes of stock hemoglobin (absorber) solution and microsphere suspensions, in deionized (DI) water with stock fluorophore solution allowed accurate control of the final absorption, scattering and fluorescence properties in each phantom. The absorption spectra of the stock HbO_2 and stock fluorophore solutions (measured using a spectrophotometer (Cary 300, Varian, Inc.) were used to determine the final absorption of the phantom, while the values of the reduced scattering coefficients in the phantoms were calculated from the Mie theory for spherical particles using freely available software. 2-NBDG (N13195, Invitrogen, Carlsbad, CA), and Rhodamine B (R6626, Sigma-Aldrich Co., St. Louis, MO) was added in increasing concentrations from 2 to 40 µM. A scattering level of 10 cm^{-1} and two different hemoglobin concentrations of 9 and 18 µM were used.

Normal mice and solid tumor studies

Six to eight week old female athymic nude mice (nu/nu, NCI, Frederic, MD) weighing 20-25 g were used in these studies. Animals were housed in an on-site housing facility with ad libitum access to food and water and standard 12-h light/dark cycles. All dosing experiments were conducted during the day and mice were fasted for 6 hours prior to optical measurements. Fasting ensured that glucose in the body did not compete with 2-NBDG uptake and good signal contrast from the tumor compared to normal tissue. Groups of 5 normal mice were injected with increasing concentrations of 2-NBDG (6, 12, 24, 36 and 48 mM). Mice in the 4T1 group received a subcutaneous injection of 750,000 4T1-RFP cells in an injection volume of 100 µl. Flank tumors were monitored every other day and allowed to grow to a volume [π/6 x length x (breadth)^2] of 200 mm^3. A total of 5 tumor-bearing animals were injected with 6 mM of 2-NBDG. A volume of 100 µl of 2-NBDG was injected systemically through the tail-vein of the mouse. For the 12 hour fasting group, mice that were fasted for 12 hours, spectroscopic measurements of reflectance and fluorescence were performed in the morning on non-fasted mice. 2 days later, mice were fasted overnight for 12 hours prior to spectroscopic measurements. Blood glucose levels were measured by a tail-vein prick using a commercially available blood glucose meter (Freestyle), prior to optical measurements. Mice were not anesthetized during measurement of blood glucose to avoid effects of isofluorane on initial blood glucose levels. During the 12-hour fasting period, animals were only provided water.

Optical spectroscopy and quantification of oxygen saturation and glucose uptake

The optical spectroscopy instrument has been described previously [96] and consists of a 450 Watt Xenon lamp coupled to a monochromator (Jobin Yvon Horiba), a fiber-optic probe

(designed in-house and custom built by RoMack Inc.), a spectrograph (Jobin Yvon Horiba), and a 2D CCD camera (Jobin Yvon Horiba). The fiber-optic probe consisted of 19 illumination fibers (diameter = 200 mm; NA = 0.22) surrounded by 18 collection fibers (diameter = 200 mm; NA = 0.22). The sensing depth of the probe was estimated from tissue-like phantoms to be approximately 1-2 mm. The optical instrument was always allowed to warm up for at least 30 minutes before initiating measurements. The optical probe was stabilized to avoid probe bending--associated changes in lamp throughput and systematic errors. Because changes in lamp throughput could affect optical measurements, reflectance and fluorescence spectra on each day were calibrated using a 20% reflectance standard (Spectralon, Labsphere) and a fluorescence reflectance standard (USF 210-010, Labsphere Inc.), respectively. Specifically, tissue reflectance spectra were divided, wavelength by wavelength, by the reflectance spectrum measured from the standard. The reflectance standard measurement also corrects the tissue reflectance spectra for the wavelength response of different system components. Fluorescence spectra were divided by the fluorescence intensity at 540 nm measured from the fluorescence standard. To correct the fluorescence spectra for wavelength response, the fluorescence spectrum from a NIST-approved tungsten calibration lamp (Optronic Laboratories Inc., Orlando, FL) was measured using the optical instrument and divided by the manufacturer-provided spectrum to obtain a correction factor. Tissue fluorescence spectra were multiplied by this correction factor to calibrate the wavelength-dependent response of the monochromators, fiber bundle and PMT. Because 1-3 mice were imaged on a given day for a total duration of 5 hours, standard measurements were performed prior to optical measurements on each mouse.

Mice were anesthetized using a mixture of isofluorane and room air (1.5% v/v) throughout the course of the optical measurements. Optical measurements were obtained by placing the fiber-optic probe on the skin covering the right flank of the mouse. Optical measurements on each mouse were acquired continuously for a period of 75 minutes. The probe was stabilized with a clamp and care was taken to ensure that pressure was not applied on tissue. Reflectance spectra were acquired from 390 – 650 nm (acquisition time: 0.05 s) and fluorescence emission spectra were acquired from 510 – 620 nm (acquisition time: 5 s) using excitation at 490 nm. Although 2-NBDG is maximally excited at ~ 475 nm, an excitation wavelength of 490 nm was used to minimize fluorescence excitation of endogenous FAD. Prior to 2-NBDG injection, baseline reflectance and fluorescence spectra were measured from the tissue site of interest. All the measurements for both phantom and animal studies were acquired in a dark room.
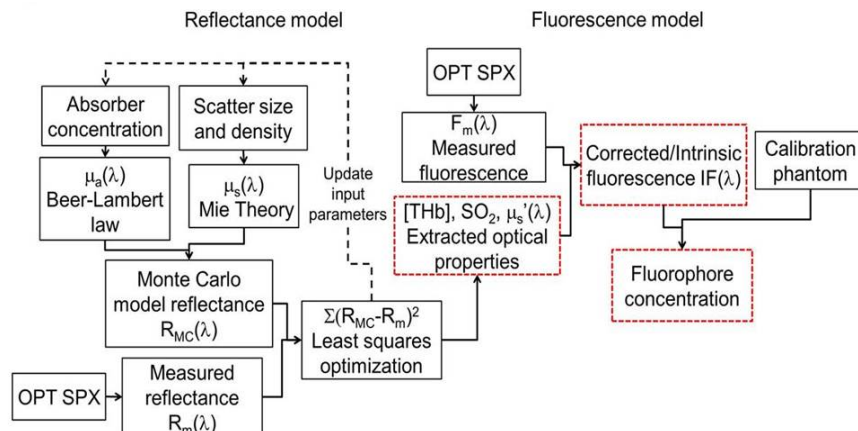
Figure 3.9: OPT-SPX instrumentation and algorithm. A. OPT-SPX instrument used to collect serial reflectance and fluorescence measurements in pre-clinical and clinical models. **B.** Flowchart describing the extraction of tissue optical properties and fluorophore concentrations. MC model of reflectance is initially fit to measured reflectance spectra to estimate optical properties such as scattering coefficient, Total hemoglobin and SO_2. These optical properties are used to remove scattering and absorption effects from measured fluorescence. The resulting intrinsic fluorescence is compared to a calibrated fluorescence tissue phantom to extract fluorophore concentrations.

A scalable inverse Monte Carlo model was used to extract tissue scattering, absorption and native fluorescence of 2-NBDG from *in vivo* optical measurements. The reflectance and fluorescence-based inverse Monte Carlo models have been described in detail previously [97-100]. Further, the fluorescence model has been validated for both single and multiple fluorophores in the sampled medium [100]. A flowchart describing the entire process is presented in **Fig. 3.9B**. Because the Monte Carlo model operates on an absolute scale and the tissue measurements are relative to a reflectance standard, a reference phantom with known optical properties is necessary to accurately scale tissue optical properties. Based on a series of phantom studies using the optical instrument and fiber-optic probe described here, a reference phantom was selected based on low errors in extracting tissue absorption and scattering. The inverse model assumes oxygenated and deoxygenated hemoglobin as absorbers and uses the widely-used extinction coefficients to calculate absorption coefficients (units of cm^{-1}). Tissue scattering is assumed to be primarily due to cells and its associated components and is calculated from scatterer size, density, and the refractive index of the scatterer and surrounding medium using Mie theory for spherical particles. The inverse component works by adaptively fitting the modeled diffuse reflectance to the measured tissue diffuse reflectance till the sum of squares error between the modeled and measured diffuse reflectance is minimized.
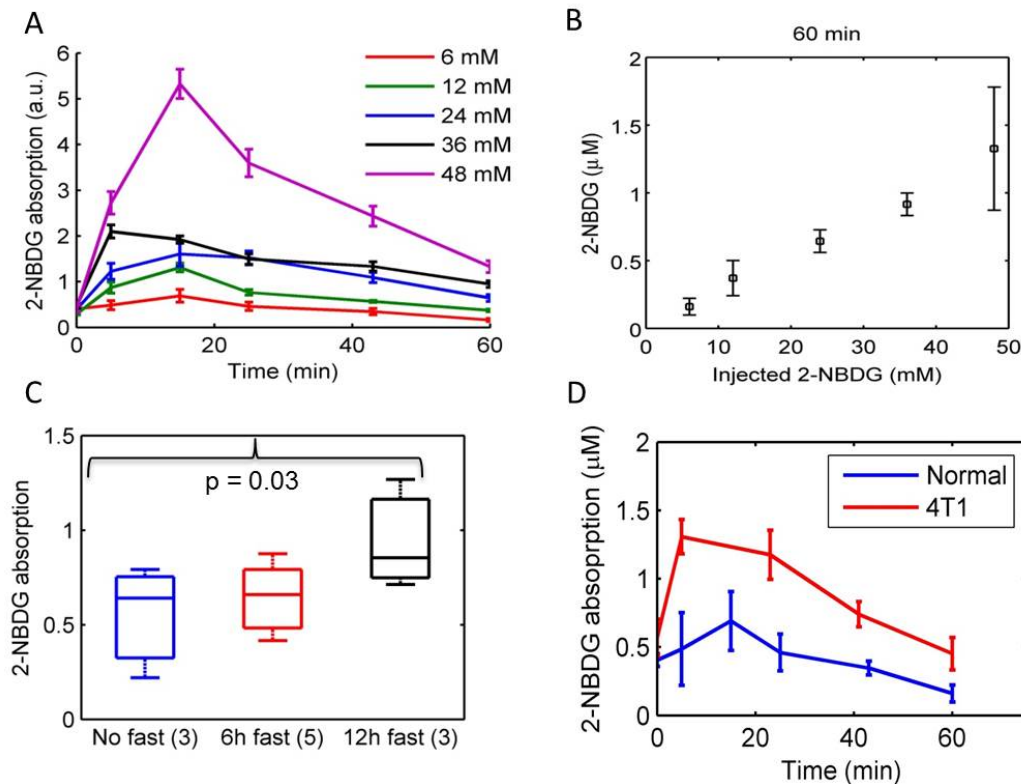
Optical spectroscopy is highly sensitive to 2-NBDG absorption *in vivo*
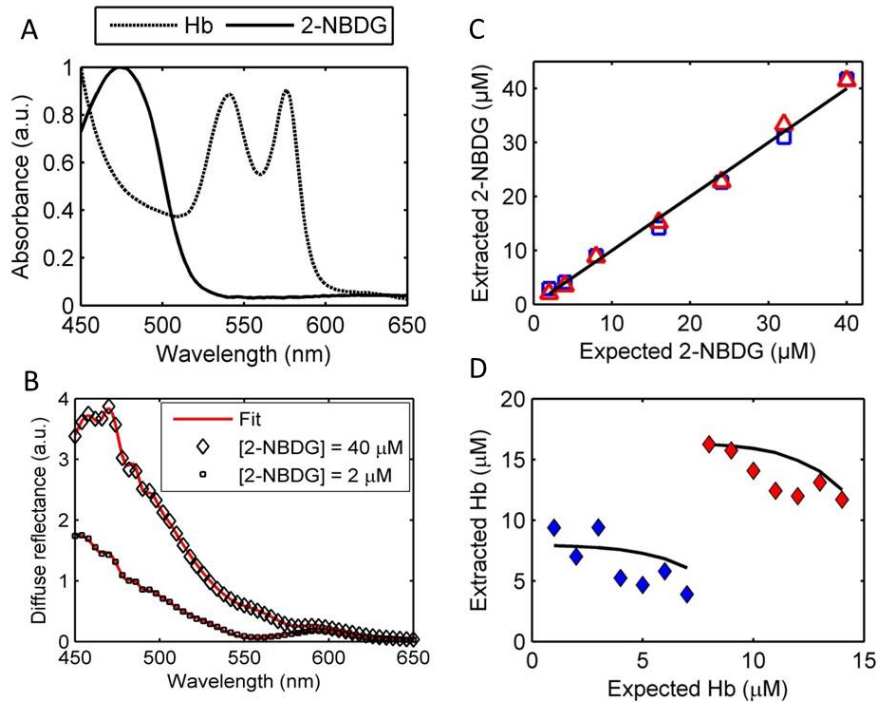
Figure 3.10: Monte Carlo inverse model can accurately extract 2-NBDG and Hb concentrations in tissue-

simulating phantoms. A. Absorption spectra of hemoglobin and 2-NBDG. **B.** Measured data and corresponding MC model fits. **C.** Extracted 2-NBDG concentrations show excellent agreement with expected 2-NBDG concentrations for different hemoglobin absorption levels. **D.** The MC model accurately extracts hemoglobin concentration in two different phantoms.

Figure 3.10 illustrates the results of applying the Monte Carlo inverse model of reflectance to tissue-simulating phantoms containing hemoglobin and increasing concentrations of 2-NBDG (2 – 40 µM). Two different hemoglobin absorption levels and the same level of scattering (polystyrene beads) were used for these experiments. The data show good fits of the MC model to the measured data, resulting in excellent measurements of [Hb] and 2-NBDG in solution. This indicates that the MC model of reflectance is highly sensitive to 2-NBDG absorption *in vivo*.

Figure 3.11: Optical spectroscopy is sensitive to 2-NBDG absorption *in vivo* A. 2-NBDG kinetics for different injected concentrations of 2-NBDG ranging from 6-48 mM. 2-NBDG absorption reaches a peak at approximately 10-15 minutes and decays to a steady state by 60 minutes. **B.** Extracted 2-NBDG absorption levels at 60 minutes for each concentration show excellent sensitivity of the technique to 2-NBDG absorption *in vivo*. **C.** Fasting increases 2-NBDG absorption in a duration-dependent manner. **D.** 2-NBDG absorption is higher in 4T1 tumors compared to normal tissue.

Figure 3.11A presents the kinetics of extracted 2-NBDG concentration as a function of injected dose. Immediately after injection, 2-NBDG concentration increases proportionate to the dose and reaches a maximum approximately 10 minutes after injection. The extracted 2-NBDG concentration then enters a period of cellular uptake, decay and clearance from tissue and reaches a steady state concentration beyond 43 minutes. **Figure 3.11B** shows the extracted 2-NBDG concentration as a function of dose at 60 minutes, demonstrating exquisite sensitivity of the reflectance model to *in vivo* changes in 2-NBDG concentration. Fasting for longer periods

increased 2-NBDG absorption proportional to the fasting duration (**Fig. 3.11C**). Specifically, fasting for 12 hours caused a significant increase in 2-NBDG absorption compared to animals that were not fasted. Finally, 2-NBDG absorption was significantly higher in 4T1 tumor xenografts relative to normal tissue (**Fig. 3.11D**).

Plans for year 5:

Our research strategy for Year 5 involves two key projects: 1. Determining the changes in glycolytic demand and vascular oxygenation in tumors in response to targeted therapy and 2. Evaluating the ability of optical imaging to measure aerobic glycolysis *in vivo*. Targeted therapies such as PI3K-inhibition can lead to significant 'normalization' of the vasculature. This can change the delivery and hence uptake of contrast agents such as 2-NBDG. Our goal is to evaluate delivery-corrected glycolytic demand in the context of therapy to determine exactly when actual glycolytic changes occur and how to separate these effects from inflammation or vasodilation which can often lead to misleading conclusions. We also plan to extend our optical spectroscopy studies to include measurements of other physiological markers such as lactate production and redox ratio. Our goal is to use a combination of endpoints to measure aerobic glycolysis *in vivo*. We will validate our toolbox or endpoints using cell lines that are known to exhibit aerobic glycolysis. We will further use this toolbox to measure the bioenergetics of therapy-resistant and therapy-sensitive tumors. Our goal at the end of Year 5 is to have a validated set of optical endpoints that report on tumor bioenergetics using both single-point spectroscopy measurements for early cancers and wide-field imaging for larger biopsy samples

3. **KEY RESEARCH ACCOMPLISHMENTS:**

   AIM 1
   - HbSat may be a useful *in vivo* parameter for determining tumor hypoxia, or for examining the local microenvironment*,* or even for margin assessment of the resected cavity*,* it is not reliable in *ex vivo* margin assessment of breast tissue specimens.
   - The results from both the simulated and phantom data for [patent blue dye] indicate that [patent blue dye] up to 80µM does not impact the extractions of [THb], [β-carotene], or $<\mu_s'>$ from the diffuse reflectance spectra.
   - In terms of tissue cauterization, we found that initial measurements of [THb] were significantly higher in the benign sites of the cauterized lumpectomies compared to the mastectomies.
   - Acquired images using the 49-channel system in 26 patients undergoing partial mastectomy or reduction mammoplasty. Of these samples, 18 have been imaged with the increased resolution raster scanning technique and pressure sensing.
   - Developed analysis software to invert diffuse reflectance measurements and process extracted parameter maps from the 49-channel system.
   - Characterizing performance metrics of the 49-channel system.

   AIM 2

   Duke
   - Continued to enroll patients in *ex vivo* biopsy study which demonstrates the potential of using HRME imaging to determine histology of samples during a core needle biopsy

procedure (n = 55 patients total). We are planning to continue enrolling patients up to n = 75 in year 5.

- Applied sparse decomposition algorithm to all images of biopsy specimens and showed potential of using it to distinguish between malignant and benign tissue.
- Outlined methodology for consolidation and classification of biopsies, and are currently optimizing our strategy to distinguish positive from negative biopsies.

Rice

- Neoplasia can be identified in confocal images with high sensitivity and specificity (Se = 93%, Sp = 93%), and neoplasia can be identified in confocal images with similar accuracy compared to review of histologic images (Se = 93%, Sp = 97%).
- The mean fluorescence intensity of DCIS (intensely stained nuclei) is higher than IDC, normal ducts, and hyperplastic ducts, all described with weakly stained nuclei
- The parameter which best identifies DCIS in histologic images is standard deviation of duct wall width, which separates DCIS from non-neoplastic ducts with a sensitivity of 78% and a specificity of 82%, corresponding to an area under the curve of 0.85. The combination of two parameters which result in the best separation between DCIS and non-neoplastic ducts are standard deviation in duct wall width and number of lumens contained within the duct wall, which identify DCIS from non-neoplastic ducts with a sensitivity of 78% and a specificity of 86%
- Parameters for quantitative analysis of duct morphology did not perform as well in identifying neoplastic lesions as subjective analysis by visual assessment; sensitivity, specificity, and AUC were lower for automated assessment in both confocal and histologic images.
- Preliminary results show that the mean size of adipocytes adjacent to invasive ductal tumors is lower than the mean size of adipocytes adjacent to DCIS foci and in normal adipose tissue

AIM 3

- Discovered significant differences in glycolytic demand and oxygenation in metastatic 4T1 tumors and non-metastatic 4T1 tumors as well as 4T1 tumors exposed to radiation.
- Developed a delivery-corrected method for measuring true glycolytic demand *in vivo.*
- Demonstrated, for the first time, serial titration and quantification of a fluorophore *in vivo.*
- Demonstrated the feasibility of combined oxygen saturation and glucose uptake *in vivo* using optical spectroscopy.

4. REPORTABLE OUTCOMES:

AIM 1:

Journal publications – (published, in review and in progress)

1. Kennedy S, Geradts J, Caldwell M, Bydlon M, Mulvey C, Mueller J, Barry W, Ramanujam N, "Using Breast Tissue Histology to Understand Optical Signatures and Improve Optical Margin Assessment." Breast Cancer Research. (*submitted*).
2. Brown, J. Q., and N. Ramanujam, "Leveraging tissue composition and micro-morpholoy or breast tumor margin assessment via quantitative diffuse optical spectral imaging", *PLoS ONE*, 2013.
3. J. Quincy Brown and Torre M. Bydlon, Stephanie A. Kennedy, Matthew L. Caldwell, Jennifer E. Gallagher, Marlee Junker, Lee G. Wilke, William T. Barry, Joseph Geradts, Nimmi Ramanujam. "Leveraging Tissue Composition and Micromorphology for Breast Tumor Margin Assessment via Quantitative Diffuse Optical Spectral Imaging," *PLoS ONE*, 2013.
4. Bydlon TM, Barry WT, Kennedy S, Brown JQ, Gallagher J, Wilke L, Geradts J, Ramanujam N.. "Advancing optical imaging for breast margin assessment: an analysis of excisional time, cautery, and patent blue dye on underlying sources of contrast." PLoS One, vol. 7, issue 12, pp. e51418, 12/2012.

AIM 2:

Journal publications – (published, in review and in progress)

1. Mueller J, Harmany Z, Mito K, Kennedy S, Kim Y, Dodd L, Geradts J, Kirsch D, Willett R, Brown Q, Ramanujam N. *Quantitative Segmentation of Fluorescence Microscopy Images of Heterogeneous Tissue: Application to the Detection of Residual Disease in Tumor Margins.* PLoS one, 2013, 8(6): e66198.
2. Fu H, Mueller J, Javid M, Mito J, Kirsch D, Ramanujam N, Brown Q. *Optimization of a Widefield Structured Illumination Microscope for Non-Destructive Assessment and Quantification of Nuclear Features in Tumor Margins of a Primary Mouse Model of Sarcoma.* PLoS one, 2013, 8(7): e68868.

Conference abstracts and proceedings

1. Mueller J, Fu H, Mito J, Javid M, Harmany Z, Dodd L, Willett R, Kirsch D, Brown Q, Ramanujam N. *Quantitative high-resolution fluorescence imaging for in vivo detection of residual disease during cancer surgery.* NCI-NIBIB Point of Care Technologies for Cancer Conference, *Bethesda, MD*, October 2013.
2. Mueller J, Harmany Z, Mito K, Kennedy S, Kim Y, Dodd L, Geradts J, Kirsch D, Willett R, Brown Q, Ramanujam N. *Quantitative segmentation of fluorescence microscopy images of heterogeneous tissue: Approach for tuning algorithm parameters.* Biomedical Spectroscopy, Microscopy, and Imaging, SPIE Photonics West Proceedings Vol. 8587, February 2013.
3. Mueller J, Harmany Z, Mito K, Kennedy S, Kim Y, Dodd L, Geradts J, Kirsch D, Willett R, Brown Q, Ramanujam N. *Quantitative segmentation of fluorescence microscopy images*

of heterogeneous tissue: Application to the detection of residual disease in tumor margins. SPIE Photonics West, *San Francisco, CA*, February 2013.

Rice

Journal publications – (published, in review and in progress)

1. Dobbs J, Shin D, Krishnamurthy S, Kuerer H, Yang W, Richards-Kortum R: Quantitative Analysis of Human Breast Morphology Associated with Progression from Non-proliferative and Hyperplastic Ducts to Ductal Carcinoma *in Situ.* (In preparation).
2. Dobbs J, Ding H, Benveniste A, Krishnamurthy S, Kuerer H, Yang W, Richards-Kortum R: Feasibility of confocal fluorescence microscopy for real-time evaluation of neoplasia in fresh human breast tissue. Journal of Biomedical Optics (In press, 2013)
3. Pierce MC, Yu D, Richards-Kortum R: High resolution fiber optic microendoscopy for in situ cellular imaging. Journal of Visualized Experiments. 2011. 47:1-4. http://www.jove.com/details.php?id=2306

Conference abstracts and proceedings

1. Dobbs J, Shin D, Krishnamurthy S, Kuerer H, Yang W, Richards-Kortum R: Quantitative Analysis of Morphology Associated with Progression from Non-proliferative and Hyperplastic Ducts to Ductal Carcinoma *in Situ* in Human Breast Tissue. Talk: *Frontiers in Optics, Optics Society of America*, 2013. Oral presentation: October 7, 2013.
2. Dobbs J, Ding H, Benveniste A, Kuerer H, Krishnamurthy S, Yang W, Richards-Kortum R: *Confocal Fluorescence Microscopy for Evaluation of Breast Cancer in Human Breast Tissue.* Poster: *Biomedical Optics and 3D Imaging Optics and Photonics Congress.* Miami, FL: Optical Society of America; 2012.
3. Dobbs J, Ding H, Benveniste A, Kuerer H, Krishnamurthy S, Yang W, Richards-Kortum R: Confocal Fluorescence Microscopy for real-time, high resolution assessment of breast cancer morphology. Poster: *Biomed OpTex Symposium.* College Station, TX, May 2012

AIM 3:

Journal publications – (published, in review and in progress)

1. Rajaram N, Frees AE, Fontanella AN, Zhong J, Hansen K, Dewhirst MW, Ramanujam N. Delivery rate affects uptake of a fluorescent glucose analog in murine models of metastatic breast cancer. *PLoS ONE* (in press), 2013.
2. Zhong J, Rajaram N, Brizel DM, Frees AE, Ramanujam N, Batinic-Haberle I, Dewhirst MW. Radiation induces aerobic glycolysis through reactive oxygen species. *Radiotherapy and Oncology* 106(1): 390-396, 2013.
3. Rajaram N, Reesor A, Mulvey CS, Ramanujam N. Reflectance spectroscopy is sensitive to absorption of a fluorophore *in vivo.* (in preparation)
4. Frees AE, Rajaram N, McCachren S, Dewhirst MW, Ramanujam N. Delivery-corrected uptake of a fluorescent glucose analog accurately measures glycolytic demand.

Conference abstracts and proceedings

1. Frees, AE, Rajaram N, McCachren S, Dewhirst MW, Ramanujam N. Optical monitoring of glucose demand and vascular delivery in a preclinical murine model SPIE Photonics West, San Francisco, CA, 2014 (accepted as a talk).
2. Rajaram N, Frees AE, Zhong J, Dewhirst MW, <u>Ramanujam N</u>. Optical imaging and spectroscopy of tumor bioenergetics. BMES Annual Meeting, Seattle, WA, Sep 25-28, 2013.
3. Rajaram N, Frees AE, Dewhirst MW, <u>Ramanujam N</u>. Optical toolbox to measure tumor bioenergetics *in vivo*. Chance Centennial Symposium, Philadelphia, PA, June 16-18, 2013.

5. CONCLUSIONS:

Aim 1

We are now characterizing the performance metrics of the 49-channel system and comparing it to the clinical criteria for intra-operative tumor margin assessment. These metrics include SNR, sensing depth, cross-talk, reproducibility, resolution, speed, drift, phantom study accuracy, and channel uniformity.

We have improved upon the system by designing and fabricating and imaging platform that enables the techniques of raster scanning and pressure sensing. The custom pressure-sensitive imaging platform allows the user to control the pressures that are maintained at the specimen to probe interface. Raster scanning allows for increased resolution by scanning interleaving spaces. LabVIEW software automates the acquisition such that user-specific error is eliminated with the motorized stage that applies pressure and performs raster-scanning. There is a trade-off between time for raster scanning and the amount of time allotted to measure in the clinic. This trade-off between time and raster scanning has been optimized such that we can image with 1.2mm resolution within the timeframe allowed in the intraoperative setting. These additions to the 49-channel system have been tested clinically on a cohort of 26 patients undergoing lumpectomy and reduction mammoplasty surgeries.

Aim 2

Duke

The *ex vivo* biopsy study demonstrates that high resolution fluorescence imaging of acriflavine stained tissue combined with an algorithm that leverages sparse decomposition analysis provides a rapid, non-destructive and automated strategy for quantitative pathology of thick tissues with non-uniform background heterogeneity. We will identify additional endpoints/parameters that have diagnostic potential, optimize our variable consolidation strategy, and build predictive models that can quantitatively diagnose high resolution images in Year 5.

Rice

The goal of this proposal was to develop and apply imaging systems and molecular contrast agents which can be used in patients to 1) improve early detection and rapid assessment of breast cancer lesions, 2) aid in selection of targeted therapeutics, and 3) monitor the efficacy of these.

Confocal fluorescence microscopy was compared to histology with H&E staining for classification of neoplastic lesions based on visual assessment and we found that readers identified neoplasia in confocal and histologic with similar accuracy. We demonstrated that mean fluorescence intensity, a parameter of confocal images, is significantly different in DCIS lesions vs. invasive carcinoma and non-neoplastic ducts.
Thus, we show that confocal images of fresh human breast tissue provide sufficient information to enable discernment of neoplastic and non-neoplastic breast features, which has potential to improve rapid assessment of breast cancer lesions

Quantitative analysis of features of breast architecture, including adipocytes and ducts, shows that there are significant differences in breast morphology at neoplastic and non-neoplastic sites. We found that adipocyte area is lower when adjacent to some lesions of invasive ductal carcinoma than in normal tissue adjacent to collagenous tissue. Quantitative parameters of duct morphology such as duct wall width, duct area, and number of lumens are associated with diagnostic categories of duct and that parameters had similar performance for classification of DCIS in both types of images. These findings indicate that physical parameters of breast morphology could be used to rapidly assess breast lesions and to monitor disease progression and regression.

Aim 3

Although a number of studies have illustrated the significance of the Warburg effect and its relationship to tumor aggressiveness, a majority was conducted in cell culture in the absence of a true microenvironment. High-resolution imaging of glucose uptake and vascular oxygenation status, as described here can provide unprecedented spatial information and help us understand the relationship between both parameters. Intravital microscopy can provide quantitative measures of *in vivo* tumor biomarkers, either endogenous or exogenous. It is non-invasive, permitting short-term repeated measurements on the same animal can continuously monitor changes in tumor microvasculature and more importantly study, at a high resolution, the cells adjacent to these blood vessels.

Our findings suggest that simply measuring glucose tracer uptake at a specific time-point is inadequate; knowledge of tracer kinetics and SO_2 as well is important to assess the tumor micro-environment. A natural follow-up to this study would be to correlate longitudinal measures of endpoints derived in this study with metastatic progression and tumor recurrence in pre-clinical models of breast cancer. Such studies could potentially provide biomarkers to predict long-term outcome in breast tumors at the time of detection.

We are currently developing and validating the endpoints derived in this study using optical spectroscopy. Optical spectroscopy affords the ability to make repeated and noninvasive *in vivo* measurements of tumor morphology and function over a long period of time. The results of this study also hold true for other imaging modalities such as PET in clinical studies and whole animal fluorescence molecular tomography (FMT) that may be used in pre-clinical studies to measure tumor glucose demand in response to therapeutic strategies such as targeted molecular agents or radiation

6. REFERENCES:

1. Jacobs, L., *Positive margins: the challenge continues for breast surgeons.* Ann Surgical Oncology, 2008. **15**(5): p. 1271-2.
2. Lee, M.C., et al., *Determinants of breast conservation rates: reasons for mastectomy at a comprehensive cancer center.* Breast J, 2009. **15**(1): p. 34-40.
3. Society, A.C. *Cancer Facts and Figures 2009*. 2009.
4. Sanchez, C., et al., *Factors associated with re-excision in patients with early-stage breast cancer treated with breast conservation therapy.* Am Surg, 2010. **76**(3): p. 331-4.
5. Mann, R.M., et al., *The impact of preoperative breast MRI on the re-excision rate in invasive lobular carcinoma of the breast.* Breast Cancer Res Treat, 2010. **119**(2): p. 415-22.
6. Balch, G.C., et al., *Accuracy of intraoperative gross examination of surgical margin status in women undergoing partial mastectomy for breast malignancy.* Am Surg, 2005. **71**(1): p. 22-7; discussion 27-8.
7. Mendez, J.E., et al., *Influence of breast cancer margin assessment method on the rates of positive margins and residual carcinoma.* Am J Surg, 2006. **192**(4): p. 538-40.
8. Huston, T.L., et al., *The influence of additional surgical margins on the total specimen volume excised and the reoperative rate after breast-conserving surgery.* Am J Surg, 2006. **192**(4): p. 509-12.
9. Kobbermann, A., et al., *Impact of Routine Cavity Shave Margins on Breast Cancer Re-excision Rates.* Ann Surg Oncol, 2010.
10. McCahill, L.E., et al., *Variability in reexcision following breast conservation surgery.* JAMA, 2012. **307**(5): p. 467-75.
11. Bydlon, T.M., et al., *Performance metrics of an optical spectral imaging system for intra-operative assessment of breast tumor margins.* Opt Express, 2010. **18**(8): p. 8058-76.
12. Wilke, L.G., et al., *Rapid noninvasive optical imaging of tissue composition in breast tumor margins.* Am J Surg, 2009. **198**(4): p. 566-74.
13. Brown, J., et al., *Optical assessment of tumor resection margins in the breast.* IEEE Journal on Selected Topics in Quantum Electronics, 2010( ): p. accepted.
14. Kennedy, S.A., et al., *Optical breast cancer margin assessment: an observational study of the effects of tissue heterogeneity on optical contrast.* breast Cancer Research, 2010. **12**(6).
15. Palmer, G.M. and N. Ramanujam, *A Monte Carlo-based inverse model for calculating tissue optical properties. Part I: Theory and validation on synthetic phantoms.* Appl. Opt., 2006. **45**(5): p. 1062-71.
16. Palmer, G.M., et al., *A Monte Carlo-based inverse model for calculating tissue optical properties. Part II: Application to breast cancer diagnosis.* Appl. Opt., 2006. **45**(5): p. 1072-8.
17. Brown, J.Q., *Optical Assesssment of Tumor Resection Margins in the Breast.* IEEE Journal of selected topics in Quantum Electronics, 2010. **16**(3): p. 530-544.

18. Bigio, I.J., et al., *Diagnosis of breast cancer using elastic-scattering spectroscopy: preliminary clinical results.* J Biomed Opt, 2000. **5**(2): p. 221-8.
19. Haka, A.S., et al., *Diagnosing breast cancer using Raman spectroscopy: prospective analysis.* J Biomed Opt, 2009. **14**(5): p. 054023.
20. Clark, A.L., et al., *Confocal microscopy for real-time detection of oral cavity neoplasia.* Clin Cancer Res, 2003. **9**(13): p. 4714-21.
21. Drezek, R.A., et al., *Optical imaging of the cervix.* Cancer, 2003. **98**(9 Suppl): p. 2015-27.
22. Nguyen, F.T., et al., *Intraoperative evaluation of breast tumor margins with optical coherence tomography.* Cancer Res, 2009. **69**(22): p. 8790-6.
23. Clark, A.L., et al., *Detection and diagnosis of oral neoplasia with an optical coherence microscope.* J Biomed Opt, 2004. **9**(6): p. 1271-80.
24. Karen, J.K., et al., *Detection of basal cell carcinomas in Mohs excisions with fluorescence confocal mosaicing microscopy.* Br J Dermatol, 2009. **160**(6): p. 1242-50.
25. Gareau, D.S., *Feasibility of digitally stained multimodal confocal mosaics to simulate histopathology.* J Biomed Opt, 2009. **14**(3): p. 034050.
26. Tanbakuchi, A.A., et al., *Clinical confocal microlaparoscope for real-time in vivo optical biopsies.* J Biomed Opt, 2009. **14**(4): p. 044030.
27. Muldoon, T.J., et al., *Subcellular-resolution molecular imaging within living tissue by fiber microendoscopy.* Opt Express, 2007. **15**(25): p. 16413-23.
28. Muldoon, T.J., et al., *High-resolution imaging in Barrett's esophagus: a novel, low-cost endoscopic microscope.* Gastrointest Endosc, 2008. **68**(4): p. 737-44.
29. Nyirenda, N., D.L. Farkas, and V.K. Ramanujan, *Preclinical evaluation of nuclear morphometry and tissue topology for breast carcinoma detection and margin assessment.* Breast Cancer Res Treat, 2010.
30. Sahoo P, S.S.a.W.A., *A survey of thresholding techniques.* Comput. Vis. Graph. Image Proc, 1988. **41**: p. 233-260.
31. Tanbakuchi, A.A., et al., *Clinical confocal microlaparoscope for real-time in vivo optical biopsies.* J Biomed Opt, 2009. **14**: p. 044030.
32. Muldoon, T.J., et al., *Subcellular-resolution molecular imaging within living tissue by fiber microendoscopy.* Opt Express, 2007. **15**: p. 16413-23.
33. Korde, V.R., et al., *Automatic segmentation of cell nuclei in bladder and skin tissue for karyometric analysis.* Anal Quant Cytol Histol, 2009. **31**: p. 83-9.
34. Tuominen, V.J., et al., *ImmunoRatio: a publicly available web application for quantitative image analysis of estrogen receptor (ER), progesterone receptor (PR), and Ki-67.* Breast Cancer Res, 2010. **12**: p. R56.
35. Ko, B., M. Seo, and J.Y. Nam, *Microscopic cell nuclei segmentation based on adaptive attention window.* J Digit Imaging, 2008. **22**: p. 259-74.
36. Wittenberg, T., et al., *A semantic approach to segmentation of overlapping objects.* Methods Inf Med, 2004. **43**: p. 343-53.
37. Zaritsky, A., et al., *Cell motility dynamics: a novel segmentation algorithm to quantify multi-cellular bright field microscopy images.* PLoS One, 2011. **6**: p. e27593.
38. Wahlby, C., et al., *Combining intensity, edge and shape information for 2D and 3D segmentation of cell nuclei in tissue sections.* J Microsc, 2004. **215**: p. 67-76.
39. Wienert, S., et al., *Detection and segmentation of cell nuclei in virtual microscopy images: a minimum-model approach.* Sci Rep, 2012. **2**: p. 503.
40. Bunyak, F., A. Hafiane, and K. Palaniappan, *Histopathology tissue segmentation by combining fuzzy clustering with multiphase vector level sets.* Adv Exp Med Biol, 2011. **696**: p. 413-24.

41.   Korzynska A, S.W.H.A.W.D.H.P., *Segmentation of microscope images of living cells.* Pattern Analysis and Applications, 2007. **10**: p. 301–319.

42.   Chan, T.F. and L.A. Vese, *Active contours without edges.* IEEE Trans Image Process, 2008. **10**: p. 266-77.

43.   Lin, G., et al., *A hybrid 3D watershed algorithm incorporating gradient cues and object models for automatic segmentation of nuclei in confocal image stacks.* Cytometry A, 2003. **56**: p. 23-36.

44.   P, V.L.a.S., *Watersheds in digital spaces: An efficient algorithm based on immersion simulations.* Trans. Pattern Anal. Mach. Intell, 1991. **13**: p. 583-598.

45.   Gonzalez, R. and R. Woods, *Digital Imaging Processing*. 3 ed. 2007.

46.   Ballard, D., *Generalizing the Hough Transform to Detect Arbitrary Shapes*. 1981, Pattern Recognition. p. 111-122.

47.   Vachier, C. and F. Meyer, *The Viscous Watershed Transform.* Journal of Mathematical Imaging and Vision, 2005. **22**: p. 251-267.

48.   Starck, J.L., M. Elad, and D.L. Donoho, *Image decomposition via the combination of sparse representations and a variational approach.* IEEE Trans Image Process, 2005. **14**: p. 1570-82.

49.   Candès, E.J. and D.L. Donoho, *New tight frames of curvelets and optimal representations of objects with piecewise C2 singularities.* Communications on Pure and Applied Mathematics, 2004. **57**: p. 219-266.

50.   Eng, J. *ROC analysis: Web-based calculator for ROC curves*. 2006 [cited 2012; Available from: http://www.jrocfit.org.

51.   YOUDEN, W.J., *Index for rating diagnostic tests.* Cancer, 1950. **3**(1): p. 32-5.

52.   Jemal, A., et al., *Global Cancer Statistics.* Ca-a Cancer Journal for Clinicians, 2011. **61**(2): p. 69-90.

53.   Siegel, R., D. Naishadham, and A. Jemal, *Cancer Statistics, 2012.* Ca-a Cancer Journal for Clinicians, 2012. **62**(1): p. 10-29.

54.   DeSantis, C., et al., *Breast cancer statistics, 2011.* Ca-a Cancer Journal for Clinicians, 2011. **61**(6): p. 409-418.

55.   Kaufman, C.S., et al., *Intraoperative ultrasound facilitates surgery for early breast cancer.* Annals of Surgical Oncology, 2002. **9**(10): p. 988-993.

56.   Kuhl, C.K., et al., *Mammography, breast ultrasound, and magnetic resonance imaging for surveillance of women at high familial risk for breast cancer.* J Clin Oncol, 2005. **23**(33): p. 8469-76.

57.   Ngo, C., et al., *Intraoperative ultrasound localization of nonpalpable breast cancers.* Annals of Surgical Oncology, 2007. **14**(9): p. 2485-2489.

58.   Sarvazyan, A., et al., *Cost-effective screening for breast cancer worldwide: current state and future directions.* Breast Cancer (Auckl), 2008. **1**: p. 91-9.

59.   Warner, E., et al., *Comparison of breast magnetic resonance imaging, mammography, and ultrasound for surveillance of women at high risk for hereditary breast cancer.* J Clin Oncol, 2001. **19**(15): p. 3524-31.

60.   Warner, E., et al., *Surveillance of BRCA1 and BRCA2 mutation carriers with magnetic resonance imaging, ultrasound, mammography, and clinical breast examination.* JAMA, 2004. **292**(11): p. 1317-25.

61.   Bobo, J.K., N.C. Lee, and S.F. Thames, *Findings from 752,081 clinical breast examinations reported to a national screening program from 1995 through 1998.* J Natl Cancer Inst, 2000. **92**(12): p. 971-6.

62.   Cerussi, A., et al., *In vivo absorption, scattering, and physiologic properties of 58 malignant breast tumors determined by broadband diffuse optical spectroscopy.* Journal of Biomedical Optics, 2006. **11**(4).

63.   Rosbach, K.J., et al., *High-resolution fiber optic microscopy with fluorescent contrast enhancement for the identification of axillary lymph node metastases in breast cancer: a pilot study.* Biomed Opt Express, 2010. **1**(3): p. 911-922.

64.   Tanamai, W., et al., *Diffuse optical spectroscopy measurements of healing in breast tissue after core biopsy: case study.* Journal of Biomedical Optics, 2009. **14**(1).

65.   Jain, M., et al., *Modified full-field optical coherence tomography: A novel tool for rapid histology of tissues.* Journal of pathology informatics, 2011. **2**: p. 28.

66.   McLaughlin, R.A., et al., *Imaging of Human Lymph Nodes Using Optical Coherence Tomography: Potential for Staging Cancer.* Cancer Research, 2010. **70**(7): p. 2579-2584.

67.   Nguyen, F.T., et al., *Intraoperative Evaluation of Breast Tumor Margins with Optical Coherence Tomography.* Cancer Research, 2009. **69**(22): p. 8790-8796.

68.   Nguyen, F.T., et al., *Optical Coherence Tomography The Intraoperative Assessment of Lymph Nodes in Breast Cancer.* IEEE Engineering in Medicine and Biology Magazine, 2010. **29**(2): p. 63-70.

69.   Parrish, A., et al., *Reflectance confocal microscopy for characterization of mammary ductal structures and development of neoplasia in genetically engineered mouse models of breast cancer.* Journal of Biomedical Optics, 2005. **10**(5).

70.   Schiffhauer, L.M., et al., *Confocal Microscopy of Unfixed Breast Needle Core Biopsies: A Comparison to Fixed and Stained Sections.* Bmc Cancer, 2009. **9**.

71.   Tilli, M.T., et al., *Real-time imaging and characterization of human breast tissue by reflectance confocal microscopy.* Journal of biomedical optics, 2007. **12**(5): p. 051901.

72.   Muldoon, T.J., et al., *High-resolution imaging in Barrett's esophagus: a novel, low-cost endoscopic microscope.* Gastrointestinal Endoscopy, 2008. **68**(4): p. 737-744.

73.   Nitin, N., et al., *Optical molecular imaging of epidermal growth factor receptor expression to improve detection of oral neoplasia.* Neoplasia, 2009. **11**(6): p. 542-51.

74.   Allred, D.C., et al., *Ductal carcinoma in situ and the emergence of diversity during breast cancer evolution.* Clin Cancer Res, 2008. **14**(2): p. 370-8.

75.   Anderson, N.H., et al., *Computerized scene segmentation for the discrimination of architectural features in ductal proliferative lesions of the breast.* J Pathol, 1997. **181**(4): p. 374-80.

76.   Campo-Ruiz, V., et al., *Evaluation of hepatic histology by near-infrared confocal microscopy: A pilot study.* Human Pathology, 2002. **33**(10): p. 975-982.

77.   Gareau, D.S., et al., *Rapid screening of cancer margins in tissue with multimodal confocal microscopy.* J Surg Res, 2012. **178**(2): p. 533-538.

78.   Pierce, M., D. Yu, and R. Richards-Kortum, *High-resolution fiber-optic microendoscopy for in situ cellular imaging.* J Vis Exp, 2011(47).

79.   Tan, J., et al., *Adipocyte is a non-trivial, dynamic partner of breast cancer cells.* International Journal of Developmental Biology, 2011. **55**(7-9): p. 851-859.

80.   Basset, P., et al., *A novel metalloproteinase gene specifically expressed in stromal cells of breast carcinomas.* Nature, 1990. **348**(6303): p. 699-704.

81.   Jodele, S., et al., *Modifying the soil to affect the seed: role of stromal-derived matrix metalloproteinases in cancer progression.* Cancer Metastasis Rev, 2006. **25**(1): p. 35-43.

82.   Wiseman, B.S. and Z. Werb, *Stromal effects on mammary gland development and breast cancer.* Science, 2002. **296**(5570): p. 1046-9.

83.   Gerlinger, M., et al., *Intratumor heterogeneity and branched evolution revealed by multiregion sequencing.* New England Journal of Medicine, 2012. **366**(10): p. 883-892.

84.   Hanahan, D. and R.A. Weinberg, *Hallmarks of cancer: the next generation.* Cell, 2011. **144**(5): p. 646-674.

85. Semenza, G.L., *HIF-1: upstream and downstream of cancer metabolism.* Current opinion in genetics & development, 2010. **20**(1): p. 51-56.

86. Warburg, O., *On the origin of cancer cells.* Science, 1956. **123**(3191): p. 309-314.

87. Hardee, M.E., et al., *Her2/neu signaling blockade improves tumor oxygenation in a multifactorial fashion in Her2/neu+ tumors.* Cancer Chemother Pharmacol, 2009. **63**(2): p. 219-28.

88. Sorg, B.S., et al., *Hyperspectral imaging of hemoglobin saturation in tumor microvasculature and tumor hypoxia development.* J Biomed Opt, 2005. **10**(4): p. 44004.

89. Zhong, J., et al., *Radiation induces aerobic glycolysis through reactive oxygen species.* Radiotherapy and Oncology, 2013. **106**(3): p. 390-396.

90. Moeller, B.J., et al., *Radiation activates HIF-1 to regulate vascular radiosensitivity in tumors: role of reoxygenation, free radicals, and stress granules.* Cancer Cell, 2004. **5**(5): p. 429-41.

91. Moeller, B.J., et al., *Pleiotropic effects of HIF-1 blockade on tumor radiosensitivity.* Cancer Cell, 2005. **8**(2): p. 99-110.

92. Rabbani, Z.N., et al., *Antiangiogenic action of redox-modulating Mn(III) meso-tetrakis(N-ethylpyridinium-2-yl)porphyrin, MnTE-2-PyP(5+), via suppression of oxidative stress in a mouse model of breast tumor.* Free Radic Biol Med, 2009. **47**(7): p. 992-1004.

93. Dewhirst, M.W., et al., *Heterogeneity in tumor microvascular response to radiation.* Int J Radiat Oncol Biol Phys, 1990. **18**(3): p. 559-68.

94. Kallman, R.F., *The phenomenon of reoxygenation and its implications for fractionated radiotherapy.* Radiology, 1972. **105**(1): p. 135-42.

95. Rajaram, N., et al., *Delivery rate affects uptake of a fluorescent glucose analog in murine metastatic breast cancer.* PloS ONE, 2013: p. in press.

96. Bydlon, T.M., et al., *Performance metrics of an optical spectral imaging system for intra-operative assessment of breast tumor margins.* Optics express, 2010. **18**(8): p. 8058-8076.

97. Palmer, G.M. and N. Ramanujam, *Monte Carlo-based inverse model for calculating tissue optical properties. Part I: Theory and validation on synthetic phantoms.* Applied optics, 2006. **45**(5): p. 1062-1071.

98. Palmer, G.M. and N. Ramanujam, *Monte-Carlo-based model for the extraction of intrinsic fluorescence from turbid media.* Journal of biomedical optics, 2008. **13**(2): p. 024017-024017-9.

99. Bender, J.E., et al., *A robust Monte Carlo model for the extraction of biological absorption and scattering in vivo.* IEEE Trans Biomed Eng, 2009. **56**(4): p. 960-8.

100. Liu, C., et al., *Experimental validation of an inverse fluorescence Monte Carlo model to extract concentrations of metabolically relevant fluorophores from turbid phantoms and a murine tumor model.* Journal of Biomedical Optics, 2012. **17**(7): p. 77012.